



THIS MANUSCRIPT HAS BEEN SUBMITTED TO THE JOURNAL OF GLACIOLOGY AND HAS NOT BEEN PEER-REVIEWED.

### Characteristics of dynamic thickness change across diverse outlet glacier geometries and basal conditions

Journal:	<i>Journal of Glaciology</i>
Manuscript ID	Draft
Manuscript Type:	Article
Date Submitted by the Author:	n/a
Complete List of Authors:	Yang, Donglai; University at Buffalo, Department of Geology; Georgia Institute of Technology, School of Earth and Atmospheric Sciences Poinar, Kristin; University at Buffalo, Geology; UB RENEW institute Crooks Nowicki, Sophie; University at Buffalo, Department of Geology; UB RENEW institute Csatho, Bea; University at Buffalo, Department of Geology
Keywords:	Ice dynamics, Glacier modelling, Ice thickness measurements, Glaciological model experiments
Abstract:	Outlet glaciers in Greenland are undergoing retreat and diffusive thinning in response to external forcings, but the rates and magnitudes of these responses differ from glacier to glacier for unclear reasons. We test how changes in ice overburden pressure and basal lubrication affect diffusive thinning rates and their spatial patterns by conducting numerical experiments over various idealized Greenland-like glacier domains. We find that ~10 km frontal retreat over a decade can produce sustained thinning rates as large as 16 m/a due to ice overburden pressure changes, at outlet glaciers with high basal drag (>60 kPa) and lateral resistive stress (>70 kPa). Localized basal lubrication perturbations induce upstream thinning and downstream thickening up to 12 m/a; the duration of the lubrication forcing generally has a greater effect than its intensity on induced thickness changes. Lastly, episodic grounding line retreats over a rough bed produce a stepped timeseries of thinning broadly consistent with observations of dynamic elevation change on

	<p>multiple Greenland glaciers. Our findings highlight the importance of local stress state changes on the spatial variation of thinning, and the critical role of grounding line position -- not ice front position -- in the total thinning over a glacier domain.</p>

SCHOLARONE™  
Manuscripts

# Characteristics of dynamic thickness change across diverse outlet glacier geometries and basal conditions

Donglai YANG<sup>1\*</sup>, Kristin POINAR<sup>1,2</sup>, Sophie NOWICKI<sup>1,2</sup>, Beata CSATHO<sup>1</sup>

<sup>1</sup>*University at Buffalo, Department of Geological Sciences, Buffalo, New York, USA*

<sup>2</sup>*University at Buffalo, RENEW Institute, Buffalo, New York, USA*

*Correspondence: Donglai Yang <donglaiy@buffalo.edu>*

**ABSTRACT.** Outlet glaciers in Greenland are undergoing retreat and diffusive thinning in response to external forcings, but the rates and magnitudes of these responses differ from glacier to glacier for unclear reasons. We test how changes in ice overburden pressure and basal lubrication affect diffusive thinning rates and their spatial patterns by conducting numerical experiments over various idealized Greenland-like glacier domains. We find that ~10 km frontal retreat over a decade can produce sustained thinning rates as large as 16 m a<sup>-1</sup> due to ice overburden pressure changes, at outlet glaciers with high basal drag (>60 kPa) and lateral resistive stress (>70 kPa). Localized basal lubrication perturbations induce upstream thinning and downstream thickening up to 12 m a<sup>-1</sup>; the duration of the lubrication forcing generally has a greater effect than its intensity on induced thickness changes. Lastly, episodic grounding line retreats over a rough bed produce a stepped timeseries of thinning broadly consistent with observations of dynamic elevation change on multiple Greenland glaciers. Our findings highlight the importance of local stress state changes on the spatial variation of thinning, and the critical role of grounding line position – not ice front position – in the total thinning over a glacier domain.

---

\*Present address: School of Earth and Atmospheric Sciences, Georgia Institute of Technology, Atlanta, Georgia, USA.

## 25 1 INTRODUCTION

26 Observations of the Greenland Ice Sheet (GrIS) mass balance over the past four decades have revealed  
27 accelerating ice loss, contributing over 10 mm to global sea-level rise (Mouginot and others, 2019). This  
28 trend is projected to continue in the twenty-first century, with high-emission scenarios likely to induce a  
29 global sea level rise of  $90 \pm 50$  mm (Goelzer and others, 2020). Mass loss is primarily driven by decreases in  
30 surface mass balance and increases in ice discharge, but precise partitioning is subject to large uncertainty  
31 in climate forcings (Fox-Kemper and others, 2023) and thus remains a target of active research. Lately,  
32 mass loss through discharge or glacier dynamics has been proposed as an important driver of mass loss in  
33 both historical observations and future projections (Mouginot and others, 2019; Choi and others, 2021).  
34 Thus, understanding the mass loss caused by the ice dynamic response to climatic forcing is critical to  
35 predicting the future evolution of the GrIS.

36 Dynamic mass change tracked via ice thickness change is primarily driven by glacier motion, via ice de-  
37 formation and basal sliding in response to stress disequilibrium, particularly due to interannual to decadal-  
38 scale changes in ice frontal geometry from calving events (Nick and others, 2009; Christian and others,  
39 2020). Over the past two decades, observations have revealed widespread retreat of outlet glaciers (Moon  
40 and others, 2020; Goliber and others, 2022) primarily caused by the intrusion of comparatively warming  
41 North Atlantic water into fjords and submarine melting at the termini (Slater and others, 2020; Wood and  
42 others, 2021). These retreats trigger ice flow accelerations and along-flow divergence, leading to thinning  
43 caused by ice dynamics that propagates upstream, in some cases penetrating dozens of kilometers inland  
44 (Pritchard and others, 2009; Wang and others, 2012; Csatho and others, 2014; Felikson and others, 2021).

45 Despite its widespread occurrence, the thinning caused by ice dynamics (hereafter referred to as dynamic  
46 thickness change) exhibits complex temporal and spatial patterns even among neighboring glaciers subject  
47 to similar oceanic forcing (McFadden and others, 2011; Csatho and others, 2014). This implies the influence  
48 of local factors, such as fjord geometries and boundary conditions. Recent studies have highlighted the  
49 role of fjord width and depth on glacier stability (Bassis and Jacobs, 2013; Enderlin and others, 2013;  
50 Carr and others, 2014; Haseloff and Sergienko, 2018; Steiger and others, 2018; Frank and others, 2022),  
51 which collectively govern the force balance structure and thus the terminus response to perturbations  
52 (Carnahan and others, 2022). Although the terminus exerts critical control over inland flow dynamics,  
53 other hydro-mechanical processes are also important, including basal hydrologic processes that regulate ice

54 flow dynamics. Basal lubrication caused by surface meltwater drainage has been extensively documented  
55 across the GrIS, resulting in seasonal acceleration and deceleration of ice flow (van de Wal and others, 2008;  
56 Bartholomew and others, 2010; Chandler and others, 2013; Kehrl and others, 2017). While most studies  
57 focus on flow velocity, dynamic thickness change caused by basal lubrication has also been observed (Bevan  
58 and others, 2015), and yet the records are comparatively sparse. Moreover, how the dynamic thickness of  
59 glaciers at various dynamical states responds to these basal perturbations remains uncharacterized (Zheng,  
60 2022). Aside from observational studies, numerical simulations generally represent basal processes via  
61 parameterization known as sliding laws. However, it remains unclear how individual terms in the sliding  
62 laws, such as the effective pressure dependence, affect the simulated dynamic thickness change and its rate  
63 of change in different geometric configurations (Joughin and others, 2019; Barnes and Gudmundsson, 2022;  
64 Felikson and others, 2022). This limitation hinders our progress in better initializing ice sheet models  
65 (Aschwanden and others, 2013) and therefore short-term projections of future ice loss (Goelzer and others,  
66 2018).

67 In this study, we examine the interplay between basal processes and glacier geometries in controlling  
68 patterns of dynamic thickness change. Specifically, we investigate two distinct types of basal perturbations  
69 that produce differing spatio-temporal impacts on ice thickness change. The first type involves variations  
70 in basal drag due to changes in ice overburden pressure. Ice overburden pressure is directly determined by  
71 the ice thickness, yet its impact on dynamic elevation change is rarely explored systematically (Habermann  
72 and others, 2013; Joughin and others, 2019). Nonetheless, it has been identified as a critical component in  
73 the tidewater glacier cycle, where frontal retreat leads to ice thinning, reduced effective pressure and basal  
74 drag, flow acceleration, and further thinning of the glacier (Benn and others, 2007; Pfeffer, 2007). The  
75 second type is a localized perturbation of basal drag at the inland portion of the glacier, most commonly  
76 due to a change in effective pressure through a change in basal pore pressure. Observational studies  
77 have shown occurrences of localized dynamic elevation change far from the terminus, possibly caused by  
78 supraglacial lake drainages or changes in basal hydrologic system (Bevan and others, 2015; Stevens and  
79 others, 2022). At fast-flowing outlet glaciers where basal sliding dominates over vertical deformation, the  
80 localized basal variability can have non-local effects on flow velocity and dynamic elevation change where  
81 theoretical consideration may fall short (Gudmundsson, 2003; Sergienko and Hulbe, 2011; Sergienko, 2013),  
82 and therefore a numerical-model-based systematic characterization of dynamic thickness change throughout  
83 the glacier domain is much needed.

84 Here we investigate these two processes using numerical experiments on various idealized Greenland-like  
85 outlet glaciers. Using idealized glacier geometries that are broadly representative of multitudes of real-world  
86 glaciers allows a generalizable study of how different forcings affect the evolution of ice-surface elevation.  
87 It minimizes the tailoring of simulations to highly specific glacier characteristics, e.g., fjord size and shape,  
88 bed topography, or basal drag. Recent studies have used idealized glacier simulation to examine glacier  
89 mass loss bias from terminus forcing temporal frequency (Felixson and others, 2022), terminus response  
90 to topographic features (Frank and others, 2022), and the impact of melt water inputs on downstream  
91 ice velocity (Poinar and others, 2019). In this study, we similarly construct a suite of idealized synthetic  
92 glaciers with variations in glacier geometric parameters and basal boundary conditions, referring to each  
93 constructed glacier as a “synthetic glacier testbed” or simply “testbed.” For each testbed, we test and  
94 characterize the impact of changes in ice overburden pressure and localized basal lubrication on dynamic  
95 thickness change.

## 96 2 METHODOLOGY

### 97 2.1 Model Setup

98 We utilized the Ice-sheet and Sea-level System Model (ISSM) to conduct the numerical experiments. ISSM  
99 is a state-of-the-art finite element package that can simulate glacier and ice-sheet scale flow dynamics  
100 (Larour and others, 2012) and we refer readers to Larour and others (2012) for details of the modeling  
101 package and governing equations. To simulate the outlet glacier flow, we employed the 2D shallow shelf  
102 approximation of ice flow physics on both grounded and floating ice. A uniform triangular meshing with a  
103 spatial resolution of 200 meters was adopted throughout the model domain (12 km × 60 km). To account  
104 for the evolution of the grounding line position, we implemented a sub-element migration scheme where  
105 the sliding law coefficient at partially grounded elements scaled with the fraction of the grounded area  
106 (Gladstone and others, 2010). While the grounding line migrates dynamically according to hydrostatic  
107 criterion, we prescribed the calving front migration enabled by the level set method in ISSM (Bondzio and  
108 others, 2016).

109 We used a time-independent surface mass balance (SMB) across all the experiments and testbeds. This  
110 is because the impact of SMB variability on ice dynamic thickness occurs at timescales longer than our  
111 decadal-scale model runs (Christian and others, 2020), precluding an ability to test SMB effects. We used  
112 Glen’s flow law with  $n = 3$  for all simulations. We assumed a uniform ice temperature of  $-3\text{ }^{\circ}\text{C}$ . Below we

113 will provide a summary of forcings, model geometry, and experimental designs. For mathematical details,  
114 please refer to the Appendix B.1.

## 115 2.2 Synthetic glacier testbeds

116 We adapted and modified the idealized Greenland outlet glacier geometry from Felikson and others (2022),  
117 which itself was based on the Marine Ice Sheet Model Intercomparison Project geometry (Asay-Davis and  
118 others, 2016, MISMIP). The calving front was initially located at 56.5 km from the influx boundary. We  
119 prescribed an across-flow bed topography similar to Felikson and others (2022), but the differences are  
120 that in our model, the bed was flat in the along-flow direction and the width of the trough  $w_c(x)$  narrowed  
121 quadratically along flow. Nonetheless, as an extended inquiry to findings we will discuss later, we also  
122 briefly investigated the influence of bed roughness on dynamic thickness change patterns (Fig. 2D), where  
123 we performed additional simulations using a bed with fractal roughness.

For model initialization, we adopted a Weertman sliding law (Weertman, 1957) describing sliding over a hard bed:

$$\tau_b(\mathbf{v}_b) = C_w^{-1/m} \|\mathbf{v}_b\|^{1/m-1} \mathbf{v}_b \quad (1)$$

124 Here  $\tau_b$  is basal shear stress,  $m$  is a prescribed constant assuming certain sliding mechanics,  $C_w$  is the  
125 prescribed Weertman law coefficient field defined in equation B.8, and  $\mathbf{v}_b$  is the sliding velocity. We used  
126 the sliding law and assumed  $m = 1$  for three primary reasons: first, its simplicity makes it the most  
127 commonly used sliding law and exponent in ice sheet modeling, and hence our findings will be relevant for  
128 modelers; second, the Weertman sliding law does not incorporate dependence on effective pressure and so it  
129 can help isolate the impact of overburden pressure on dynamic thinning; third, the Weertman sliding law is  
130 valid at the high effective pressure limit, as both the Schoof and Tsai sliding law formulations (Schoof, 2005;  
131 Tsai and others, 2015) asymptotically approach the Weertman formulation at higher effective pressure.

132 To construct a suite of testbeds, we varied the width  $W$  of the fjord at the narrower end, the grounding  
133 line depth  $B_{gl}$  (zero at sea level), and the sliding law coefficient  $C_w$ , producing in total 18 testbeds as  
134 illustrated in Fig. 1. To the first order, the prescribed sliding law coefficient magnitudes control mean  
135 basal drag levels near the termini (Table 3).

136 We relaxed the testbed glaciers for 500 simulation years to allow them to reach their steady state, which  
137 we defined as  $dh/dt < 0.01m a^{-1}$  everywhere in the flow domain. At steady state, testbed glaciers with  
138 shallower grounding line depths were grounded across the whole domain, whereas testbeds with deeper

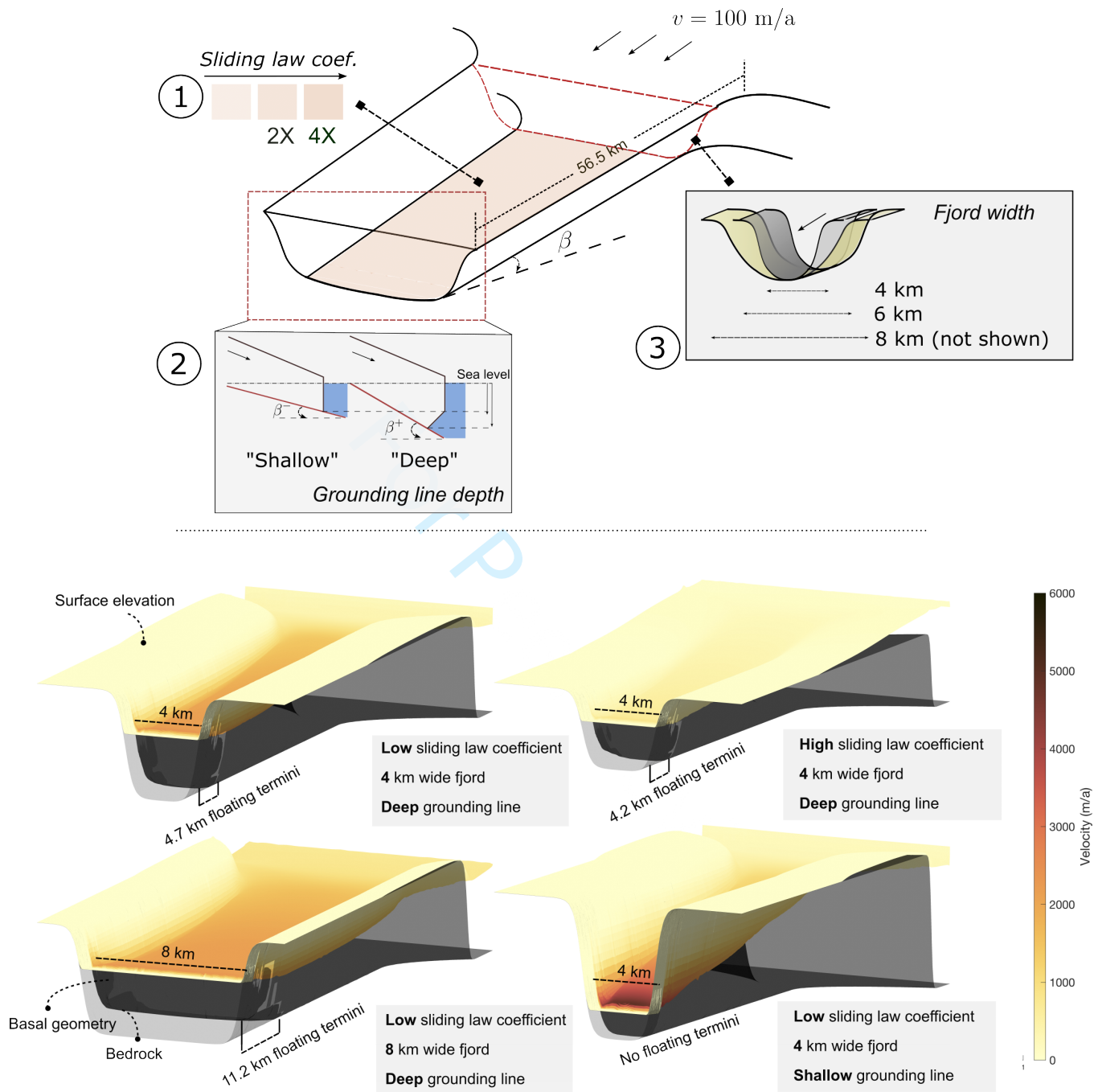


**Fig. 1.** Synthetic testbeds and examples. Top panel shows three variables of interests. 1 - Sliding law coefficient. 2 - Grounding line depth and frontal geometry. 3 - Fjord width. With the flow domain length fixed, the grounding line depth is adjusted via changing bedrock slope  $\beta$ , where testbeds with deep grounding line and floating termini (“Deep”) have greater bed slope ( $\beta^+ = -0.012$ ), and the ones with shallow grounding lines and fully grounded termini (“Shallow”) have lesser bed slope ( $\beta^- = -0.005$ ). Four examples of testbeds are shown in the bottom panel, with the steady-state ice speed colored and superimposed on the surface.



139 grounding lines depth developed floating sections up to 12 km long (Fig. 1 and Table 2). This is broadly  
140 consistent with Greenland outlet glaciers (Hill and others, 2018). For simplicity, we refer to glaciers with  
141 deep grounding lines and floating termini as “deep testbeds,” and their fully grounded shallow counterparts  
142 with shallow grounding lines as “shallow testbeds.” The 18 testbeds differ significantly in their average and  
143 maximum flow velocity near the terminus (Fig. 1 and Table 3).

## 144 **2.3 Experiment Design**

### 145 *2.3.1 Control run*

146 Previously studies have shown strong correlation between the evolution of terminus position and flow  
147 dynamics in certain glaciers (Nick and others, 2009; Cheng and others, 2022), but simulating terminus  
148 motion is known to be a challenging task due to a variety of under-constrained processes involved (Benn  
149 and others, 2007; Bassis and Jacobs, 2013; Robel, 2017; Slater and others, 2017; Choi and others, 2018;  
150 Slater and others, 2019; An and others, 2021). Therefore in this study, we did not aim to reproduce a  
151 sequence of terminus position comparable to observational records. Instead, we forced the terminus in all  
152 testbeds to retreat identically throughout all the experiments.

153 After a testbed glacier is initialized to its steady state, we forced the calving front to retreat at a time-  
154 variable rate described by a triangular function that spans 16 years (grey box in Fig. 2A). The calving  
155 front experiences an accelerating retreat for eight years, decelerates for eight years, and stabilizes. We  
156 designed this pattern to represent a smoothed-step decadal retreat of a calving front, broadly similar to  
157 the observed terminus retreats of many outlet glaciers around GrIS in the past twenty years, where the  
158 early 2000s marked the onset of widespread retreat, followed by a period of relative stability in the late  
159 2000s through early 2010s (Khazendar and others, 2019).

### 160 *2.3.2 Overburden pressure experiment*

The basal drag of a glacier depends on the contact area between the ice and the bedrock. It is regulated  
by a competition between opening of cavities from sliding over bumps or melting and creep closure of ice  
(Cuffey and Paterson, 2010; Schoof, 2010), which manifests as varying effective pressure. To account for  
the dependence on the pressure, a sliding law alternative to Weertman’s law, commonly known as Budd’s

Constant parameters in synthetic testbeds and experiments				
Symbol	Definition and unit	Value		
$\phi$	Maximum reduction of sliding law coefficient in localized basal perturbation	0.8		
$\kappa$	Ratio of Gaussian basal perturbation width to fjord width	0.08		
$B_0$	Bed elevation at influx boundary (m)	100		
$t_d$	Characteristic timescale of diffused pulse (a)	1.3		
$t_p$	Characteristic timescale of transient pulse (a)	0.1		
$f_c$	Characteristic width of channel side walls (m)	400		
$x_0$	Distance of the localized Gaussian perturbation to influx boundary (m)	32,000		
$d_c$	Depth of the trough relative to the top of side walls (m)	1000		
$x_f$	Funnel-shape characteristic length (m)	15,000		
$\rho_i$	Ice density ( $\text{kg m}^{-3}$ )	917		
$v_m$	Maximum frontal retreat rate ( $\text{m a}^{-1}$ )	1000		
$L_x$	Model domain length (m)	60,000		
$L_y$	Model domain width (m)	12,000		
$t_s$	Year to start calving front perturbation (a)	5		
$t_e$	Year to end calving front perturbation (a)	21		
Variable parameters in synthetic testbeds				
Symbol	Definition and unit	Low	Mid	High
$B_{gl}$	Grounding line elevation for model initialization (m).	-200	/	-600
$C_{wo}$	Weertman sliding law coefficient in the flow trunk for model initialization ( $\text{kg m}^{-2} \text{s}^{-1}$ )	30,000	60,000	120,000
$W$	Width of the fjord (m)	4000	6000	8000

**Table 1.** Parameters in synthetic testbeds and experiments. “Variable parameters” refers to values of a variable that differs across synthetic testbeds. Readers can refer to Table 2 in the supplementary material for the parameters grouped by each testbed.

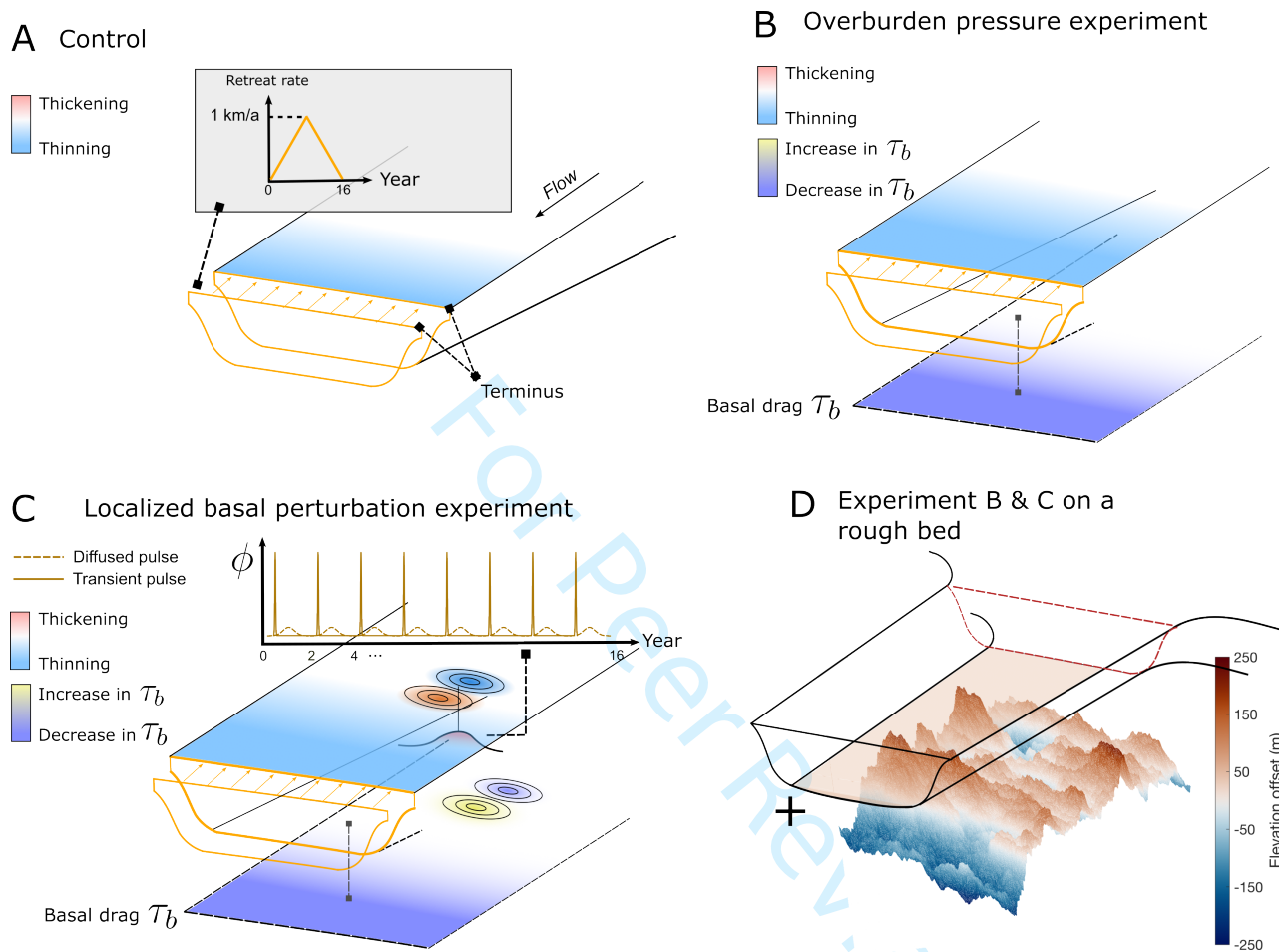


**Fig. 2.** Testbeds and experiment designs. A) Control run. The terminus is forced to retreat at a time-variable rate according to the triangular function (orange). B) Overburden pressure experiment. The basal drag  $\tau_b$  decreases as a result of diffusive thinning from the retreating terminus. C) Localized basal perturbation experiment. In addition to changes in overburden pressure due to thinning, a Gaussian-shaped region of lower sliding law coefficient is applied transiently 24.5 km upstream of the terminus. The magnitudes  $\phi$  of the two types of temporal variability (“Transient pulse” and “Diffused pulse”) are shown in brown. The perturbation locally induces upstream thinning (blue) and downstream thickening (red). D) Experiment with a rough bed. Zero in the elevation offset means no change with respect to the original constant bed slope. Both the overburden pressure and localized basal perturbation experiment are repeated on a testbed glacier with a rough bed.

law (Budd and others, 1979), is used:

$$\tau_b = C_b^2 N^{q/m} \|\mathbf{v}_b\|^{1/m-1} \mathbf{v}_b \quad (2)$$

161 where  $C_b$  is the coefficient for the Budd sliding law. In Budd's formulation, initial thinning near the glacier  
 162 terminus will reduce the ice overburden pressure and hence the effective pressure  $N$ , reducing the basal drag  
 163 and causing acceleration. The acceleration can lead to flux divergence that further reduces the effective  
 164 pressure, potentially precipitating a positive feedback.

We investigated the impact of the varying overburden pressure on dynamic thinning and hence we refer to this experiment as the "overburden pressure experiment." This is effectively the same simulation as the control run but with Budd sliding law instead. After initializing the testbed glacier with Weertman sliding law, we forced the terminus to retreat in the same fashion as in the control run. To avoid explicitly switching the sliding law in the program, we modified the sliding law coefficient of Weertman sliding law to represent Budd sliding law. By equating equation 2 and equation 1, we iteratively adjusted the basal drag coefficient  $C_w$  to compensate for changes in ice overburden pressure:

$$C_w(x, y, t) = \sqrt{C_{wo}^2 + \hat{C}_w^2 ([\rho_i g H(x, y, t)]^{1/m} - [\rho_i g H(x, y, 0)]^{1/m})} \quad (3)$$

165 where  $\rho_i$  is the ice density,  $t = 0$  in the parentheses represents field values at steady state, and  $\hat{C}_b$   
 166 is the equivalent Weertman sliding law coefficient in Budd's formulation at steady state, i.e.,  $\hat{C}_w =$   
 167  $C_{wo}/(\rho_i g H(x, y, 0))^{1/m}$ . In all experiments outlined in Fig. 2 we assumed  $m = q = 1$ . Nonetheless we  
 168 also explored a more plastic bed rheology (i.e.,  $m = 5$ , Figure 10) and compared results to the linear  
 169 viscous case in the discussion.

### 170 2.3.3 Localized basal perturbation experiment

171 In addition to overburden pressure change discussed above, we considered the impact due to local drainage  
 172 of melt water to the bed. It was represented ideally by a localized basal drag reduction as a Gaussian-  
 173 shaped patch of lower sliding law coefficient, centered 24.5 km behind the initial calving front. We used  
 174 this location because it was immediately upstream of the most retreated grounding line in our control runs,  
 175 so that the localized perturbation remained engaged throughout the simulations.

176 We considered two types of temporal variability, Transient Pulse and Diffused Pulse, to represent the

177 temporal variation of perturbation magnitude (Fig. 2C). Transient Pulse is a short-lived perturbation  
178 lasting for 0.1 year, which we designed to loosely represent the response of an efficient subglacial drainage  
179 system to supraglacial lake drainage or a rain event. The Diffused Pulse spanned a 2-year period with a  
180 lower peak value and integrated to the same total slipperiness perturbation as the Transient Pulse (Equation  
181 B.12). We chose a 2-year period as a bounding case to provide a substantial contrast with the Transient  
182 Pulse signal. It was not designed based on observations of any specific glaciers, although we would discuss  
183 certain observations and model inferences that suggest a similarly prolonged period of reduced basal drag.  
184 There are a total of eight perturbation cycles and hence 16 years of perturbation.

## 185 **2.4 Bed constructed with fractal roughness**

186 Glacier beds around GrIS are wavy at a range of length scales. This waviness is well characterized by fractal  
187 roughness (Jordan and others, 2017), meaning the asperity height at various wavelengths can be described  
188 by a Hurst exponent in a power law. To investigate the impact of bed roughness on dynamic thickness  
189 change, we generated a randomly rough surface superimposed onto a sloped flat bed (Mona Mahboob  
190 Kanafi, 2023), with a Hurst exponent of 0.8 and a root-mean-square roughness of 70 meters (Fig. 2D).  
191 Similar values were used by Christian and others (2022) for the GrIS and are within the range of roughness  
192 estimates from radar observation (Jordan and others, 2017). The specified mean roughness stipulates the  
193 average height of bed bumps; in our glacier domain, the bumps that the grounding line retreats over are  
194 less than 100 meters in height. The results are discussed in Sect. 4.1.2.

## 195 **2.5 Estimating frontal resistive stress loss**

196 The diverse geometries and mean basal drag levels considered produce various stress balance regimes and  
197 changes in stress balance in response to the calving front and grounding line retreat. To quantitatively assess  
198 the changes, we follow the calculation outlined in van der Veen and Whillans (1989) and Carnahan and  
199 others (2022) to estimate the stress components. The stress balance states that the gravitational driving  
200 stress of a glacier is approximately in balance with the sum of the basal shear stress, the longitudinal, and  
201 lateral resistive stress gradients.

202 We define the frontal resistive stress as the sum of the lateral, longitudinal, and basal resistive stress  
203 from the current grounding line to the ice front. Hence, we define the frontal loss of resistive stress as the  
204 total change in the resistive stress over the duration of the model runs. Mathematical details are presented

205 in the Appendix B.4. The results are discussed in Sect. 4.2.

## 206 **3 RESULTS**

### 207 **3.1 Overburden pressure experiment**

208 As the terminus retreats, in all testbeds, dynamic thinning originated near the terminus and diffused  
209 upstream, and the largest degree of thinning was found behind the grounding line. If we isolate the thinning  
210 induced by overburden pressure feedback, for fully grounded testbed glaciers with shallower grounding lines,  
211 the sliding law correction for ice overburden pressure added a maximum of 97 meters over 16 years, or  
212  $6 \text{ m a}^{-1}$  (Fig. 3) and all grounding lines remained grounded throughout (e.g., Fig. 3A). Model testbeds  
213 with deep grounding lines (Fig. 3B-D) showed a substantially larger degree of thinning accompanied by  
214 continued grounding line retreat. The deep narrow testbed with high basal drag (Fig. 3D) showed the  
215 most thinning, 250 meters over the 16 year model run, or an average thinning rate of  $16 \text{ m a}^{-1}$ .

216 The colored circles in Fig. 3 illustrate how the maximum  $dh/dt$  and attenuation distance vary across  
217 fjord widths, mean basal drag levels, and frontal geometries. Attenuation distance is defined as distance  
218 from ice front where the cumulative thickness change has dropped to 36.8% (e-folding length  $1/e$ ) of total  
219 thickness change. At all testbed glaciers, attenuation distance was primarily controlled by the mean basal  
220 drag: high basal drag corresponded to larger thickness change attenuation, and vice versa. Maximum  
221 thinning rate, however, exhibited a more nuanced relationship with geometry and basal condition. At  
222 testbed glaciers with high mean basal drag (e.g., mean basal drag near the terminus  $> 60 \text{ kPa}$  in Table  
223 3), the effect of fjord width was more pronounced, with narrow testbed experiencing greater maximum  
224 thinning rate up to  $16 \text{ m a}^{-1}$  despite less grounding line retreat, and wide testbed experiencing  $< 10 \text{ m a}^{-1}$   
225 thinning. Conversely, at testbeds with lower mean basal drag (e.g., mean basal drag  $< 30 \text{ kPa}$  in Table 3),  
226 differences in fjord width did not result in variances in max thinning rate ( $10.4 - 10.5 \text{ m a}^{-1}$ ).

### 227 **3.2 Localized basal perturbation experiment**

228 We present the results of the localized basal perturbation experiment as their difference in dynamic thick-  
229 ness change from the control run. In other words, we isolate the thinning caused by the localized basal  
230 perturbation alone. Immediately after it is introduced, the perturbation caused transient thickening on  
231 the downstream glacier and transient thinning on the upstream portion, regardless of the magnitude or  
232 duration of the forcing (Fig. 4 and Fig. 5). This dipole pattern is consistent with the results of previous

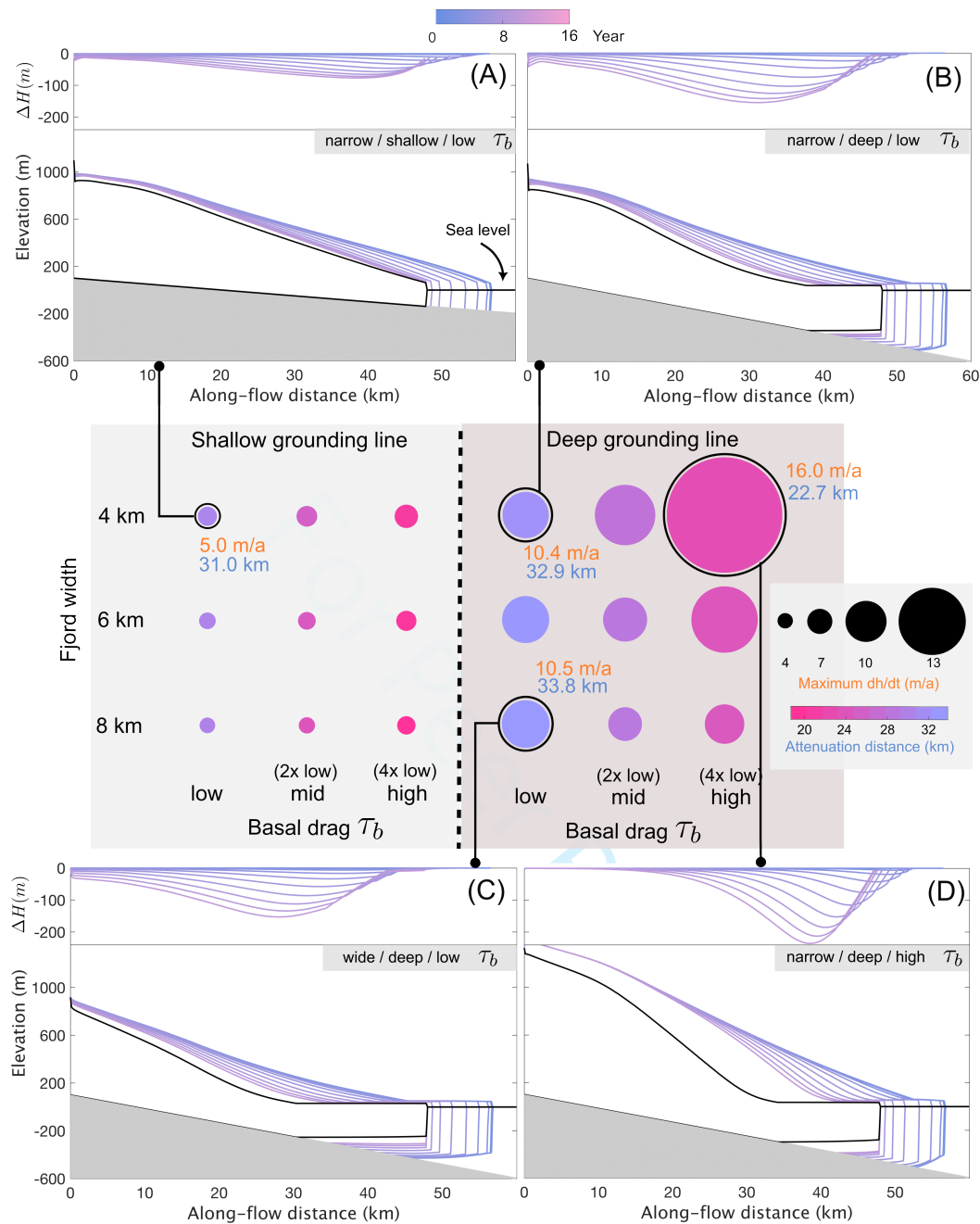


**Fig. 3.** Dynamic thickness change due to changes in ice overburden pressure. All 18 testbeds are represented as colored circles in a  $3 \times 6$  grid separated by the grounding line depths. The circular marker represents both the maximum  $dh/dt$  observed along the center flow line (marker size) and the attenuation distance of diffusive thinning (color). Shorter attenuation distance suggests stronger thinning attenuation. All values can be found in Table 5 and Table 6. Four selected testbed glaciers are shown in greater details. The lateral profiles show total thinning from the overburden pressure experiment, whereas the line plot at the top of each subplot shows the thickness change isolated ( $\Delta H$ ) from the effect of ice overburden pressure (i.e., overburden pressure experiment minus control in Fig. 2). Black lines show the lateral profiles at the new steady states.

233 theoretical studies (Gudmundsson, 2003; Sergienko and Hulbe, 2011; Sergienko, 2013).

234 Over multiple perturbation cycles, the amplitude of the transient response increased as ice flow sped  
235 up and the glacier thinned. The maximum observed thinning or thickening did not exceed 20 meters  
236 with respect to the state before the perturbation engaged. Within each perturbation cycle, thickening and  
237 thinning at the site relaxed more quickly in testbed glaciers with lower mean basal drag and, consequently,  
238 higher flow speeds. Between testbeds, the dipole amplitudes showed amplitude differences less than 12  
239 meters near the perturbation site (Table 4). At both deep and shallow testbed glaciers, we observed  
240 generally similar patterns in the dipole amplitude and its temporal variation. Therefore, for simplicity of  
241 presentation, we show results of the localized basal perturbation experiment for only the deep testbeds, and  
242 all the ensuing qualitative discussions apply to shallow testbed glaciers as well unless indicated otherwise.  
243 Results from selected shallow testbeds can be found in the Appendix (Fig. 12 and Fig. 13).

244 Over time, trends in dynamic thickness change emerged both near and far from the perturbation site.  
245 Persistent thinning occurred 5–15 km upstream of the perturbation, while downstream, variable patterns of  
246 thickening and thinning occurred at different testbeds. At testbeds with lower mean basal drag, thinning  
247 propagated farther outward from the perturbation site, whereas at testbeds with higher mean basal drag,  
248 these attenuated closer. The total degree of far-field thinning over the long term depends on the type of  
249 perturbation pulse used, with the diffused pulse resulting in generally twice as much thinning or thickening  
250 as the transient pulse.

251 More substantial differences in spatio-temporal patterns can be observed in the downstream trunk,  
252 particularly after several perturbation cycles. We present a few examples here. For the narrow testbed with  
253 a low mean basal drag level (Fig. 4A), the basal perturbation incited initial thickening in the downstream  
254 trunk that was, within ~10 years, overridden by the diffusive thinning from the trunk upstream. Similarly,  
255 in the first five years of the experiment, the grounding line advanced slightly before retreating by about  
256 40 m, relative to the control run. A qualitatively similar pattern can be observed in the narrow testbed  
257 with a high mean basal drag level (Fig. 4B), but in this case, net thinning (relative to the control run)  
258 emerged near the grounding line after the third perturbation cycle. This thinning reached ~3 m and  
259 diffused upstream; unlike in the low-basal-drag testbed, the thinning continued after the perturbations  
260 ceased, spreading throughout the domain.

261 When forced with the diffused pulse, these two testbeds exhibited similar spatial and temporal patterns  
262 (Fig. 4C and D). However, there was more thickening and less thinning and the grounding lines advanced



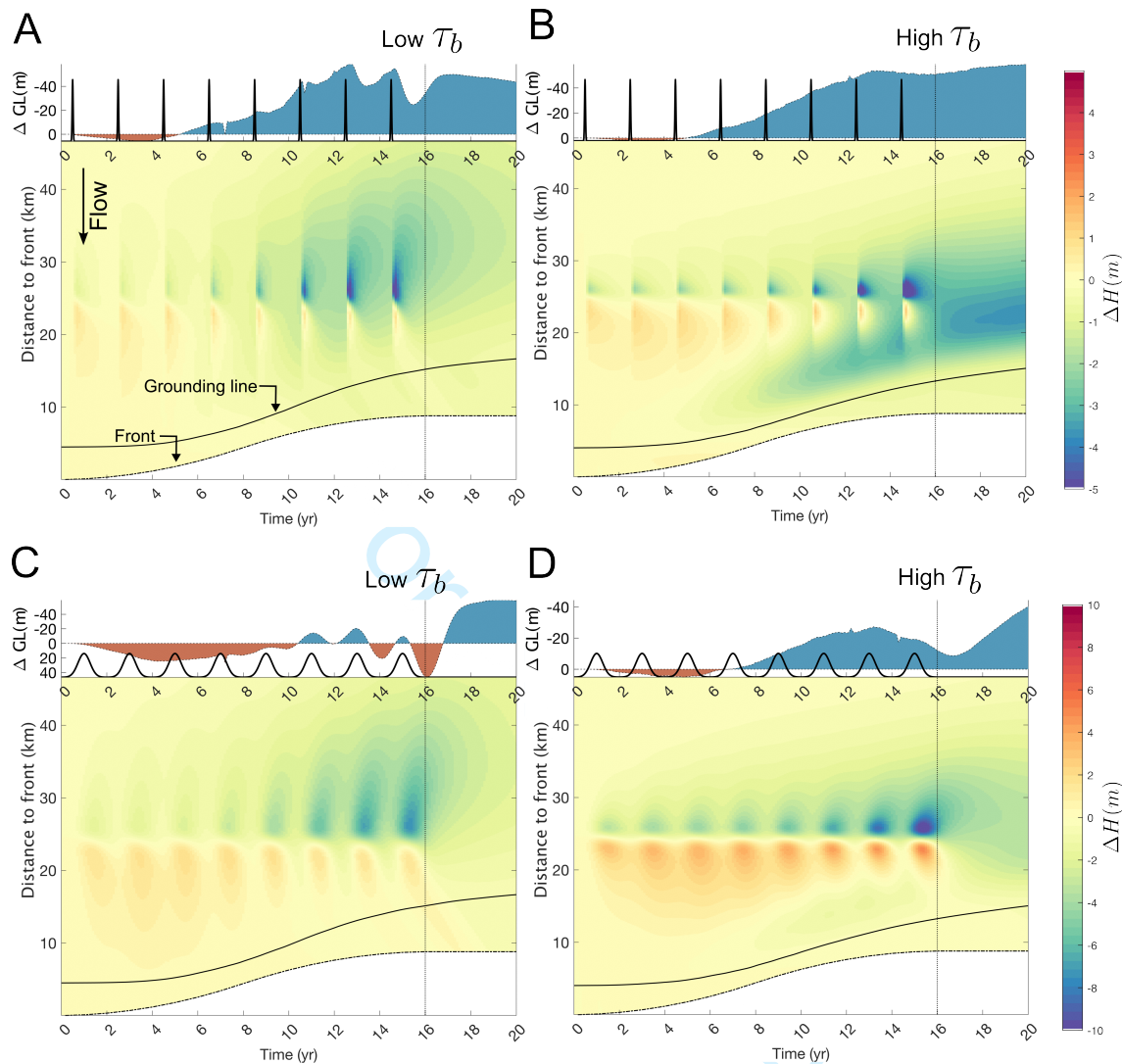


**Fig. 4.** Spatio-temporal patterns of dynamic thickness change at **deep and narrow** testbed glaciers in response to the two types of localized basal perturbation pulses. The space-time plots (essentially a Hovmöller diagram) are created by plotting the thickness change (colors) along the center flow line (y-axis) over time (x-axis). All the results presented here account for the changes in ice overburden pressure on the basal drag. The relative grounding line position on the top plots (labeled “ $\Delta GL(m)$ ”) is the difference in grounding line position between the control run and the experiment run. The Y-axis label “Distance to front” refers to the ice front location at  $t = 0$ . The thin vertical dotted line marks the end of frontal retreat. The two types of pulse forcings are shown at the top in each panel. The amplitudes of the pulses are illustrative and thus not to scale. A) A testbed glacier with low mean basal drag ( $\tau_b$ ) forced with Transient Pulse. B) A testbed glacier with high  $\tau_b$  forced with Transient Pulse. C) A testbed glacier with low  $\tau_b$  forced with Diffused Pulse. D) A testbed glacier with high  $\tau_b$  forced with the Diffused Pulse.

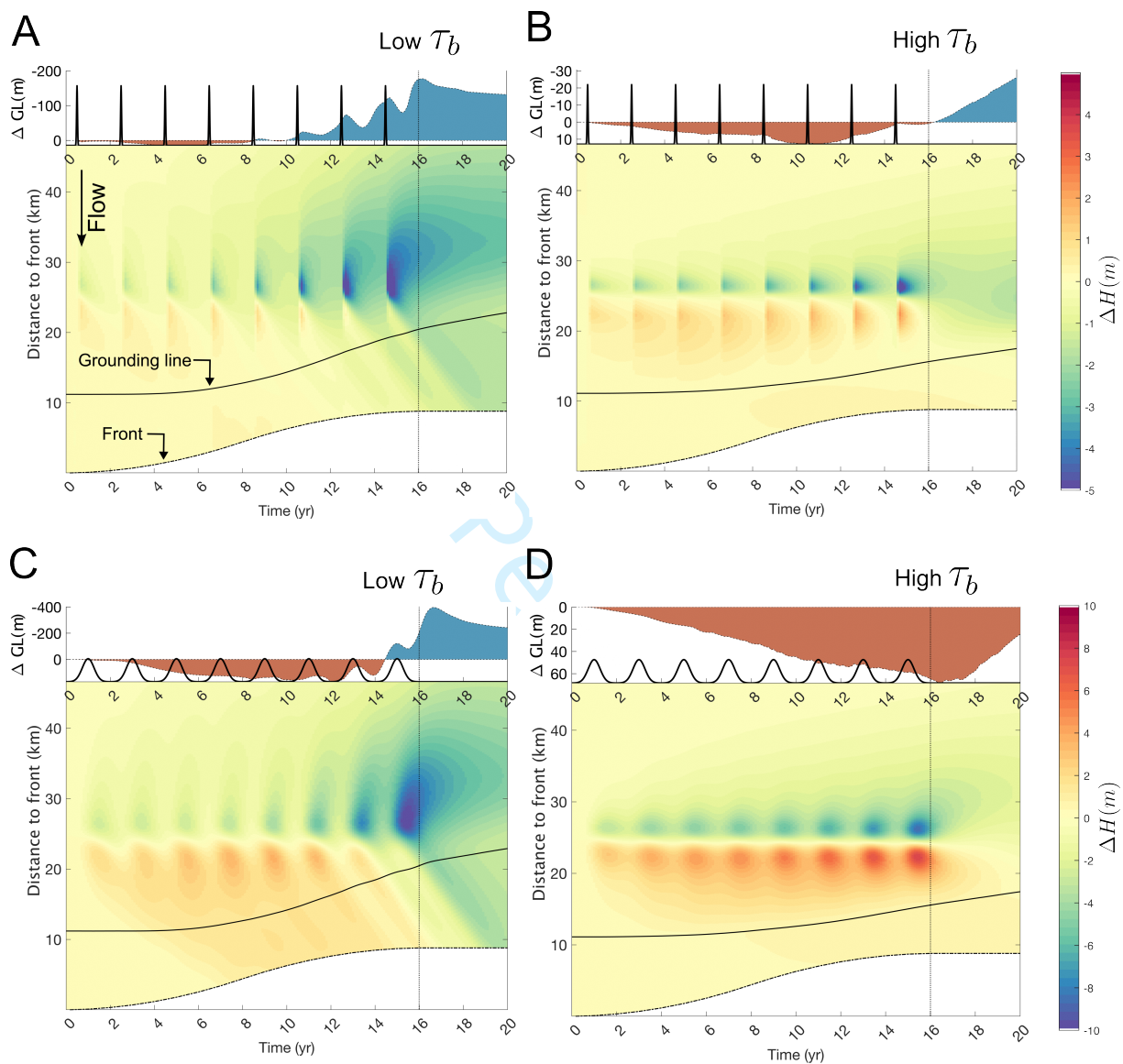


**Fig. 5.** Spatio-temporal patterns of dynamic thickness change at **deep and wide** testbed glaciers in response to the two types of localized basal perturbation pulses. Graphic features are identical to Fig. 4. A) A testbed glacier with low mean basal drag ( $\tau_b$ ) forced with Transient Pulse. B) A testbed glacier with high  $\tau_b$  forced with Transient Pulse. C) A testbed glacier with low  $\tau_b$  forced with Diffused Pulse. D) A testbed glacier with high  $\tau_b$  forced with Diffused Pulse.

263 farther.

264 Figure 5 shows results on wide testbeds. Here, the spatio-temporal patterns were generally similar to  
265 those observed in narrow testbeds, except that the upstream and downstream thickness changes were more  
266 polarized, with the upstream dominantly thinning and the downstream dominantly thickening throughout  
267 the perturbation cycles (with the minor exception of the low-basal-drag testbed in Fig. 5A). An extreme  
268 example is the testbed glacier with a high mean basal drag level forced with the diffused pulse (Fig. 5D),  
269 where the downstream thickening was not overtaken by upstream thinning years after the perturbation had  
270 stopped (in contrast to Fig. 5C, for example). It is noteworthy that the grounding lines in testbed glaciers  
271 with a low basal drag level (Fig. 5A and C) moved much more rapidly and extensively, with advance and  
272 retreat ranging from approximately 200 to 400 meters – an order of magnitude greater than in high-basal-  
273 drag testbeds. In all experiments, regardless of patterns, the maximum thickness change caused by the  
274 localized basal perturbation did not exceed 12 meters over the 26 years of simulation run (see Table 4).

## 275 4 DISCUSSION

### 276 4.1 Grounding line position correlates with dynamic thinning

#### 277 4.1.1 Experiments on a flat bed

278 Our experiments show that the grounding line positions correlate well with dynamic thinning rates. This  
279 is in contrast to ice front position, a commonly used observable in both modeling and observational studies  
280 (Bondzio and others, 2017; Kehrl and others, 2017). We ran all testbed simulations with the same ice front  
281 position forcing, but obtained a wide range of thinning degrees and variabilities (Fig. 3, 4, 5), suggesting  
282 the limited predictive power of ice front position alone. Most thinning is observed behind the grounding  
283 line, as model results for Pine Island Glacier also showed (Joughin and others, 2019).

284 We observed continued grounding line retreat even after the calving front stopped retreating. This  
285 continued retreat is associated with the large thinning difference between the shallow and deep glaciers  
286 when the basal drag coefficient is adjusted to compensate for changes in ice overburden pressure (Fig. 3).  
287 Similar dynamics were observed at Kangerlussuag Glacier (Kehrl and others, 2017) where the termini  
288 stabilized but the glacier continued to thin dynamically as the grounding line retreated, even as the glacier  
289 rested on a prograde bed.

290 The movement of the grounding line is highly dependent on the choice of sliding law (Brondex and

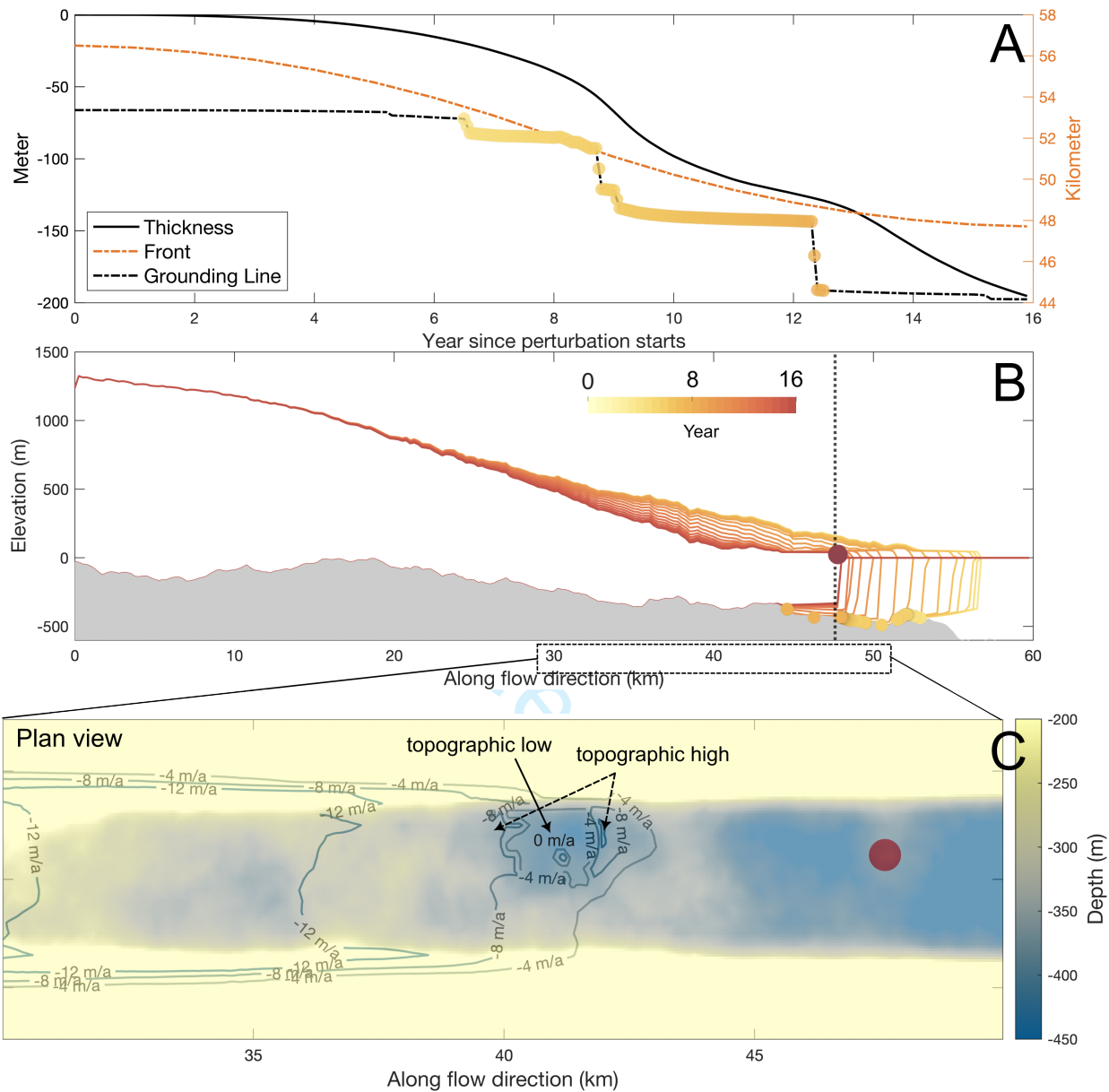


**Fig. 6.** Dynamic thickness change over an undulating bed. A) Ice thickness, grounding line, and calving front change over time. Smooth multi-year front retreat causes step changes in grounding line, temporally matching the periods of faster and slower dynamic thinning. Timeseries are extracted at the location marked as a red circle in B and C. Colored dots over the grounding line reference the same color bar in B. B) Lateral profiles of basal topography and ice surface elevation. C) Dynamic thickness change rate (contours) at the last time step superimposed onto the basal topography (colors) near the ice front and grounding line. Ice at the central topographic low becomes ungrounded and experiences low thinning rate; ice at the topographic high nearby undergoes a much higher thinning rate, illustrating spatially heterogeneous thinning rates controlled by topographic variability.

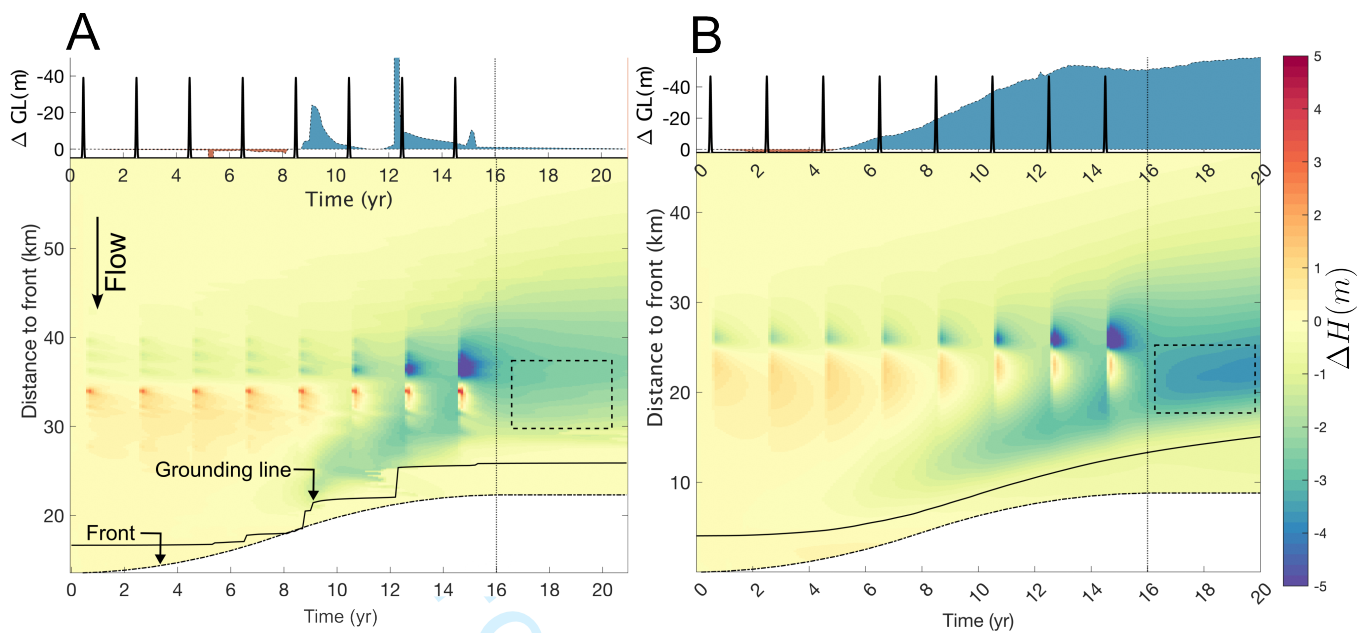


**Fig. 7.** Comparing dynamic thickness change over a flat and an undulating bed forced by localized basal perturbation. Dotted line box outline the time and space where thinning diverges after perturbation stops. A) Isolated thickness change due to the localized basal perturbation at a rough bed. B) Same but at a flat bed (Fig. 4B repeated).

291 others, 2017). Therefore, knowledge of the specific bed rheology and sliding mechanics is crucial to accu-  
 292 rately reproduce grounding line movements from observations. Our experiments with the Weertman and  
 293 Budd sliding laws are two bounding cases for the magnitude of grounding line retreat (Brondey and others,  
 294 2017). In that study, greater retreat distance of the grounding line was found to correlate with greater  
 295 thinning; our results reproduce this finding for multiple glacier geometries and mean basal drag levels.

296 The crucial role of grounding lines in dynamic thickness change is also highlighted in our localized  
 297 basal perturbation experiments. We found that, across testbed glaciers of varying widths and sliding  
 298 laws, downstream elevation change patterns strongly correlate with relative grounding line movement.  
 299 One striking example is the pronounced thinning near the grounding line as the grounding line retreats  
 300 relative to its initial position (e.g., Fig. 4B). This thinning nearly overtakes the local thickening signal  
 301 immediately downstream of the perturbation near the end of the experiment. Similarly, continued relative  
 302 grounding line advance causes downstream thickening (e.g., Fig. 5D). Despite repeated forcing, the diversity  
 303 of grounding line movements and dynamic thickness change patterns suggests that one must consider both  
 304 grounding line movement and glacier geometry when interpreting thickness change records, with all else  
 305 assumed equal. We note that, although the magnitude of dynamic thickness change from the localized basal  
 306 perturbation experiment is much smaller than other experiments (e.g., maximum thinning summarized in

307 Table 4), the critical role of grounding line movement we identified implies that more dramatic elevation  
308 change triggered by localized basal perturbation near the grounding line is possible with different basal  
309 topographic variability (Thomas and others, 2009). At a minimum, we stress the role of the grounding line  
310 in initiating dynamic thickness change, even if the perturbation is localized tens of kilometers upstream of  
311 the calving front.

#### 312 *4.1.2 Effect of basal topography variability*

313 The corollary of our finding is that dynamic thickness change must correlate more strongly with the ground-  
314 ing line motion than with terminus motion (Fig. 9). Due to the asymmetry of grounding line flux dynamics  
315 at prograde and retrograde sections of the bed (Schoof, 2007), an idealistic smooth terminus retreat can  
316 translate into episodes of fast and slow grounding line movement as it retreats over bed asperities, po-  
317 tentially giving rise to a different timescale of variability in dynamic thickness change timeseries observed  
318 across GrIS (Csatho and others, 2014). We explored this possibility with two additional simulations of the  
319 overburden pressure experiment and localized basal perturbation experiment, using a testbed with high  
320 mean basal drag in a narrow fjord with fractal roughness throughout the bed (Fig. 2D). The resulting  
321 grounding line movement is characterized by step-wise retreats, corresponding to faster and slower periods  
322 of thickness change (Fig. 6A and Fig. 7). We also observe that grounding line retreat stabilizes on the lee  
323 side of the bed bump (Fig. 6A and B) that stops further thinning after calving front perturbation ceases,  
324 in contrast to the original flat bed simulation (Fig. 7B).

325 For the rough bed, dynamic thickness change rates also exhibit spatial heterogeneity. Here we observe  
326 the topographic low behind grounding line attains flotation near the end of simulation (Fig. 6C) and the  
327 thinning rate dwindles, at  $0 - 4 \text{ m a}^{-1}$ , while its neighboring topographic high experiences  $8 - 12 \text{ m a}^{-1}$   
328 of thinning. The variation in thickness change rates across space, as revealed by simulations, presents  
329 an intriguing opportunity for utilizing consistent and precise ice surface elevation reconstructions (e.g.,  
330 altimetry data fusion engine SERAC as described in Schenk and Csathó (2012)) to gain insights into  
331 fundamental geophysical phenomena like glacier ungrounding and subglacial lake dynamics.

## 332 **4.2 Controls of resistive stress on the spatial variation of dynamic thinning**

333 In most cases, grounding line position can be readily extracted from elevation observations on glaciers with  
334 well-known bed topography and fjord bathymetry. Our results show that while the grounding line position

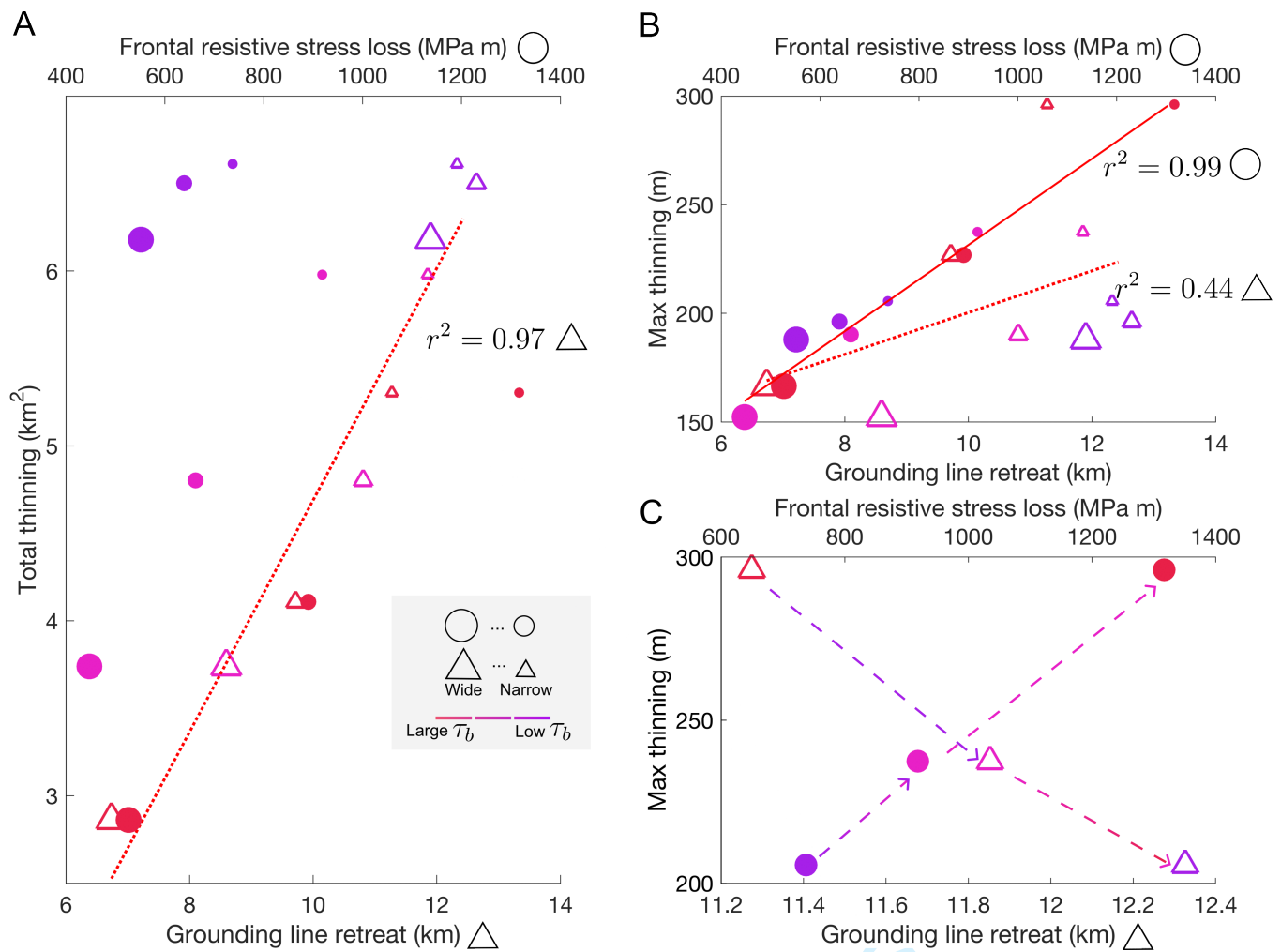


**Fig. 8.** Relationships between total thinning, maximum thinning, grounding line retreat, and frontal resistive stress loss at the end of perturbations (simulation year = 16) for deep testbeds in the overburden pressure experiment. Each marker represents a distinct testbed. R-squared values report the goodness of fit of selected data by a linear regression model. A) Relationship between total thinning versus grounding line retreat distance (triangles), and total thinning versus frontal resistive stress loss (circles). B) Relationship between the spatial maximum thinning rate and grounding line retreat distance (triangles) and frontal resistive stress loss (circles). C) Detail of (B) with only the three testbeds with narrow fjords. The dashed lines with arrows point to testbeds of increasing mean basal drag. Sizes of markers are enlarged with respect to B) for better presentation.

335 is strongly correlated with centerline-integrated total thinning and average thinning rate (Fig. 8A), it gives  
336 far less insight into the spatial pattern of thinning, here represented by spatial maximum in thinning  
337 (Fig. 8B). We hypothesize that resistive stress state is the more important variable for spatial variations  
338 in thinning.

339 The spatial maximum in thinning should be a function of the magnitude of resistive stress change near  
340 the ice front. Our results (Fig. 8B) indeed show a positive correlation between these quantities ( $r^2 = 0.99$ );  
341 in contrast, grounding line retreat does not correlate strongly with maximum thinning ( $r^2 = 0.44$ ). Fig. 8C  
342 shows that specifically at testbeds with narrow fjords, lower mean basal drag testbed produces greater  
343 grounding line retreat, yet lower spatial maxima in thinning. In fact, at narrow fjords, grounding line  
344 retreat anti-correlates with the spatial maxima in thinning; this is not the case in moderate-width and wide  
345 testbeds, as shown in the trends across sets of the larger-sized triangles in Figure 8B. Although this may  
346 seem counter-intuitive, the force balance response differs across different frontal and grounding line retreat  
347 outcomes. Specifically, calving of fully grounded testbed glaciers removes basal resistive stress, whereas at  
348 a floating terminus, the loss of the longitudinal stress gradient associated with calving is typically orders of  
349 magnitude less. Therefore, for the same prescribed terminus retreat, fully grounded testbed glaciers should  
350 experience more thinning. Indeed, observations of grounded outlet glaciers in West Greenland suggest  
351 that fully grounded glaciers undergo higher-magnitude dynamical changes than those with floating termini  
352 (McFadden and others, 2011). Furthermore, most GrIS outlet glacier fjord widths observed by Wood and  
353 others (2021) are similar to our 4 km narrow testbed (Fig. 14). Thus, knowledge of the glacier stress state  
354 is likely necessary to explain locally observed high-magnitude thinning.

355 Further evidence of the sensitivity of basally supported glaciers to grounding line retreat can be observed  
356 in the localized basal perturbation experiment. At testbed glaciers with high mean basal drag, pervasive  
357 thinning originating near the grounding line (as seen near year 10 in Fig. 4B) highlights this sensitivity.  
358 In contrast, testbeds with low basal stress (e.g., Fig. 4A) undergo the same magnitude of grounding line  
359 retreat yet lack this diffusive thinning. The potential for higher-stressed glaciers to undergo dramatic  
360 thinning echoes the modeled high sensitivity of the ice loss at East Antarctic Ice Sheet to a basal thermal  
361 state transition, where inversions identify large basal areas with high basal drag (Dawson and others, 2022).



### 362 4.3 Longer-duration basal perturbations incite greater thickness changes

363 The localized basal perturbation experiment emulates two types of drainage efficiency (Moon and others,  
364 2014), which produce contrasting examples of dynamical thickness changes both near and far downstream  
365 of the perturbation. The diffused pulse, which is a basal drag reduction whose peak value is 10 times less  
366 than its transient counterpart, actually induces a larger magnitude of thickening/thinning immediately  
367 downstream/upstream of the perturbation. Furthermore, it prolongs the initial grounding line advance  
368 period, resulting in continued downstream thickening, which is particularly visible in wide testbeds (Fig. 5).  
369 These results emphasize the disproportionately larger impact of extended basal drag reduction on the glacier  
370 state.

371 The reasons for a long-lasting lower basal drag can be diverse. For instance, modeling of Helheim  
372 hydrology shows elevated pore pressure and low effective pressure during winter from frictional dissipation  
373 from high sliding speed (Sommers and others, 2023). A subglacial drainage system may fail to channelize  
374 due to insufficient meltwater discharge or lack of meltwater forcing variability (Schoof, 2010), or high ice-  
375 overburden pressure limits sizes of cavity (Doyle and others, 2014; de Fleurian and others, 2016), although  
376 the latter is more likely to occur in the accumulation zone where ice thickness is over 1 km. Additionally,  
377 multi-year inversions on surge glaciers experiencing thermal state switches triggered by surface meltwater  
378 have inferred basal drag changes on inter-annual timescales (Dunse and others, 2015; Gong and others,  
379 2018). The synthetic pulses spanning 0.1 and 2 years used in this study can also be interpreted as lower  
380 and upper bounds of timescale, and efficient drainage can develop over a variety of timescales (Vijay and  
381 others, 2021). Generally, the disproportionately larger impact from a long-lasting perturbation should not  
382 be overlooked. Additionally, previous investigations into the drainage system efficiency on flow dynamics  
383 have focused primarily on ice velocity patterns. We complement this knowledge by suggesting that, when  
384 interpreting the dynamic elevation change records, future studies should also consider the possible impact  
385 of prolonged basal lubrication even if the total magnitude of basal lubrication is relatively small.

### 386 4.4 Propagation of diffusive thinning

387 In our testbeds, mean basal drag level primarily and fjord width, to a lesser extent, control ice velocity  
388 (Table 3). For example, the narrow testbed with a high mean basal drag has a maximum flow speed of  
389 less than 1 km per year, which is only 30% of the speed of its low-mean-basal-drag counterpart. The speed  
390 at which the diffusive thinning propagates from the terminus roughly scales with how quickly diffusive

391 thinning can propagate, which is typically 5-8 times the ice flow velocity (van de Wal and Oerlemans, 1995;  
392 van der Veen, 2001). With high ice velocity due to low mean basal drag, longitudinal stretching rapidly  
393 transmits upstream and leads to widespread thinning. A similar mechanism has been proposed to explain  
394 far-reaching inland acceleration at Jakobshavn Isbræ due to low basal drag (Bondzio and others, 2017).

395 Previous studies (Felikson and others, 2017, 2021) have used Peclet numbers to identify large undula-  
396 tions in basal topography, known as “knickpoints” as limits to upstream thinning propagation. While this  
397 offers a valuable static map view of where diffusive thinning diminishes, our simulations show that glacier  
398 dynamics conditioned by geometry and basal conditions determines the spatial extent of thinning on a  
399 decadal timescale, which may occur far downstream of major knickpoints in real-world glaciers (e.g., near  
400 the grounding line). Our results complement previous studies by suggesting that glacier dynamic state  
401 and its evolution can also play a considerable role in mapping upstream thinning extent. Furthermore,  
402 our simulations show that while glaciers with low mean basal drag can propagate diffusive thinning far  
403 inland, similar to gentle bed topography discussed in Felikson and others (2021), glaciers with narrow  
404 fjords and higher mean basal drag levels can lose almost the same amount of mass during the same period  
405 (the smallest magenta dot in Fig. 8A), despite its strong thinning attenuation which concentrates behind  
406 the grounding line. The more delayed recovery of grounding line retreat after the front stops retreating  
407 suggests that these glaciers may have even higher mass loss potential (e.g., the black profile of Fig. 3D  
408 testbed at its new steady state).

#### 409 **4.5 Implications for ice sheet modeling**

410 Our work has useful implications for future modeling studies. We have shown in Fig. 3 that thinning  
411 magnitude depends sensitively on the sliding law, where an addition of ice overburden pressure feedback  
412 causes large variability in thinning. The choice of exponent in the sliding law may also add uncertainty to  
413 projected ice loss. To explore the effect of the exponent, we perform one additional overburden pressure  
414 experiment where we set  $m = 5$ , corresponding to a more plastic bed where increase in sliding velocity has  
415 more limited impact on the basal drag strengthening. Simulation results (Fig. 10) show that the thinning  
416 pattern and magnitude resemble more the Weertman case (without overburden pressure dependence), and  
417 difference in grounding line migration from the control run in Fig. 3 is negligible. This can also be seen  
418 from equation 3 where in the limit of perfect plasticity, i.e.,  $m \rightarrow \infty$ , the sliding law coefficient  $C$  remains  
419 constant and thus is effectively Weertman sliding law. This suggests substantial differences in ice mass

420 loss projection due to the choice of the exponent alone in the same sliding law. Since Weertman and Budd  
421 sliding law remain the most commonly employed sliding laws in glacier and ice sheet scale modeling (e.g.  
422 Bondzio and others, 2017; Goelzer and others, 2020; Dawson and others, 2022) our results echo previous  
423 finding that sliding laws can critically influence ice mass loss projections (Brondex and others, 2017).  
424 Our work contributes to the knowledge by showing that in a wide range of glacier geometries and basal  
425 boundary conditions, grounding line is a decent proxy for total dynamic thinning (Fig. 8A), and therefore  
426 grounding line movement can potentially be used as a constraint to calibrate the choices of sliding law  
427 when initializing large-scale ice sheet models.

428 Additionally, it is important for studies using idealized glacier setups to be cautious when initializing  
429 glaciers with steady-state frontal geometries, such as fully grounded or floating termini. Our simulations  
430 reveal substantial thinning differences between glaciers with deep or shallow grounding lines (Fig. 11),  
431 which can bias the identification of primary controls suggested in Felikson and others (2022), for instance.

## 432 5 CONCLUSION

433 Our study explores the effect of ice overburden pressure and local basal slipperiness perturbations on  
434 dynamic thickness change of Greenland-like testbed glaciers, in an effort to constrain potential factors that  
435 may be driving dynamic thickness changes across Greenland glaciers.

436 We find that changes in both overburden pressure and basal slipperiness can induce dynamic thickness  
437 change which correlates well with grounding line migration. We find relationships between grounding line  
438 position and domain-wide thinning, and between front-to-grounding-line resistive stress loss and maximum  
439 thinning rate, but we find great variability from testbed to testbed in dynamic thinning rates despite  
440 consistent ice-front position histories. Thus, although ice-front position is readily observable, it should be  
441 used with caution for prediction or diagnosis of glacier dynamic thinning patterns.

442 We find changes in ice overburden pressure alone can be responsible for over 100 meters of dynamic  
443 thinning as terminus continuously retreats over a decade, particularly at glaciers with narrow fjords and  
444 high basal drag levels. Basal lubrication perturbations have a diagnostic dipole shape that could be  
445 identified in maps of  $dh/dt$ . The time duration of a basal forcing has greater efficacy on surface elevation  
446 than its magnitude.

447 Finally, we find that on wavy-bedded glaciers, a uniform retreat of a calving front can produce episodic  
448 grounding line retreats, which manifest as short-duration undulations in dynamic elevation. In light of

449 all these findings, we stress the importance of incorporating knowledge of bed topography, grounding line  
450 locations, and stress estimates in any interpretation of observed dynamic thickness changes.

## 451 6 DATA AVAILABILITY

452 The scripts to run ISSM simulations and recreate the figures can be found on GitHub (<https://github.com/alastairyang/ThinningTestbedPublic.git>). The simulation output data is available on Zenodo  
453 (<https://doi.org/10.5281/zenodo.10564805>). ISSM is publicly available at <https://issm.jpl.nasa.gov/>.  
454  
455

## 456 7 ACKNOWLEDGEMENTS

457 This work was supported by NASA Cryospheric Sciences grant “Integration of ICESat-2 Observations into  
458 Ice Sheet Elevation Change Records to Investigate Ice Sheet Processes” (80NSSC21K0915). We thank  
459 Climate Data Toolbox (Greene and others, 2019) and Scientific colour maps (Cramer, 2018) for their data  
460 visualization tools.

## 461 REFERENCES

- 462 An L, Rignot E, Wood M, Willis JK, Mouginot J and Khan SA (2021) Ocean melting of the Zachariae Isstrøm  
463 and nioghalvfjærdsfjorden glaciers, northeast Greenland. *Proceedings of the National Academy of Sciences of the*  
464 *United States of America*, **118**(2), e2015483118, ISSN 10916490 (doi: 10.1073/PNAS.2015483118/SUPPL{  
465 }FILE/PNAS.2015483118.SD01.XLSX)
- 466 Asay-Davis XS, Cornford SL, Durand G, Galton-Fenzi BK, Gladstone RM, Hilmar Gudmundsson G, Hattermann  
467 T, Holland DM, Holland D, Holland PR, Martin DF, Mathiot P, Pattyn F and Seroussi H (2016) Experimental  
468 design for three interrelated marine ice sheet and ocean model intercomparison projects: MISMIP v. 3 (MISMIP  
469 +), ISOMIP v. 2 (ISOMIP +) and MISOMIP v. 1 (MISOMIP1). *Geoscientific Model Development*, **9**(7), 2471–  
470 2497, ISSN 19919603 (doi: 10.5194/GMD-9-2471-2016)
- 471 Aschwanden A, Aøalgeirsdóttir G and Khroulev C (2013) Hindcasting to measure ice sheet model sensitivity to initial  
472 states. *Cryosphere*, **7**(4), 1083–1093, ISSN 19940416 (doi: 10.5194/tc-7-1083-2013)
- 473 Barnes JM and Gudmundsson GH (2022) The predictive power of ice sheet models and the regional sensitivity of  
474 ice loss to basal sliding parameterisations: a case study of Pine Island and Thwaites glaciers, West Antarctica.  
475 *Cryosphere*, **16**(10), 4291–4304, ISSN 19940424 (doi: 10.5194/TC-16-4291-2022)

- 476 Bartholomew I, Nienow P, Mair D, Hubbard A, King MA and Sole A (2010) Seasonal evolution of subglacial drainage  
477 and acceleration in a Greenland outlet glacier. *Nature Geoscience* 2010 3:6, **3**(6), 408–411, ISSN 1752-0908 (doi:  
478 10.1038/ngeo863)
- 479 Bassis JN and Jacobs S (2013) Diverse calving patterns linked to glacier geometry. *Nature Geoscience* 2013 6:10,  
480 **6**(10), 833–836, ISSN 1752-0908 (doi: 10.1038/ngeo1887)
- 481 Benn DI, Hulton NR and Mottram RH (2007) ‘Calving laws’, ‘sliding laws’ and the stability of tidewater glaciers.  
482 *Annals of Glaciology*, **46**, 123–130, ISSN 0260-3055 (doi: 10.3189/172756407782871161)
- 483 Bevan SL, Luckman A, Khan SA and Murray T (2015) Seasonal dynamic thinning at Helheim Glacier. *Earth and*  
484 *Planetary Science Letters*, **415**, 47–53, ISSN 0012-821X (doi: 10.1016/J.EPSL.2015.01.031)
- 485 Bondzio JH, Seroussi H, Morlighem M, Kleiner T, Rückamp M, Humbert A and Larour EY (2016) Modelling calving  
486 front dynamics using a level-set method: Application to Jakobshavn Isbræ, West Greenland. *Cryosphere*, **10**(2),  
487 497–510, ISSN 19940424 (doi: 10.5194/TC-10-497-2016)
- 488 Bondzio JH, Morlighem M, Seroussi H, Kleiner T, Rückamp M, Mouginit J, Moon T, Larour EY and Humbert A  
489 (2017) The mechanisms behind Jakobshavn Isbræ’s acceleration and mass loss: A 3-D thermomechanical model  
490 study. *Geophysical Research Letters*, **44**(12), 6252–6260, ISSN 19448007 (doi: 10.1002/2017GL073309)
- 491 Brondex J, Gagliardini O, Gillet-Chaulet F and Durand G (2017) Sensitivity of grounding line dynamics to the choice  
492 of the friction law. *Journal of Glaciology*, **63**(241), 854–866, ISSN 0022-1430 (doi: 10.1017/JOG.2017.51)
- 493 Budd WF, Keage PL and Blundy NA (1979) Empirical Studies of Ice Sliding. *Journal of Glaciology*, **23**(89), 157–170,  
494 ISSN 0022-1430 (doi: 10.3189/S0022143000029804)
- 495 Carnahan E, Catania G and Bartholomäus TC (2022) Observed mechanism for sustained glacier retreat and acceler-  
496 ation in response to ocean warming around Greenland. *The Cryosphere*, **16**(10), 4305–4317, ISSN 1994-0424 (doi:  
497 10.5194/TC-16-4305-2022)
- 498 Carr JR, Stokes C and Vieli A (2014) Recent retreat of major outlet glaciers on Novaya Zemlya, Russian Arctic,  
499 influenced by fjord geometry and sea-ice conditions. *Journal of Glaciology*, **60**(219), 155–170, ISSN 00221430 (doi:  
500 10.3189/2014JoG13J122)
- 501 Chandler DM, Wadham JL, Lis GP, Cowton T, Sole A, Bartholomew I, Telling J, Nienow P, Bagshaw EB, Mair  
502 D, Vinen S and Hubbard A (2013) Evolution of the subglacial drainage system beneath the Greenland Ice Sheet  
503 revealed by tracers. *Nature Geoscience* 2013 6:3, **6**(3), 195–198, ISSN 1752-0908 (doi: 10.1038/ngeo1737)

- 504 Cheng G, Morlighem M, Mouginot J and Cheng D (2022) Helheim Glacier's Terminus Position Controls Its Seasonal  
505 and Inter-Annual Ice Flow Variability. *Geophysical Research Letters*, **49**(5), e2021GL097085, ISSN 1944-8007 (doi:  
506 10.1029/2021GL097085)
- 507 Choi Y, Morlighem M, Wood M and Bondzio JH (2018) Comparison of four calving laws to model Greenland outlet  
508 glaciers. *Cryosphere*, **12**(12), 3735–3746, ISSN 19940424 (doi: 10.5194/tc-12-3735-2018)
- 509 Choi Y, Morlighem M, Rignot E and Wood M (2021) Ice dynamics will remain a primary driver of Greenland ice sheet  
510 mass loss over the next century. *Communications Earth & Environment*, **2**(1) (doi: 10.1038/s43247-021-00092-z)
- 511 Christian JE, Robel AA, Proistosescu C, Roe G, Koutnik M and Christianson K (2020) The contrasting response  
512 of outlet glaciers to interior and ocean forcing. *Cryosphere*, **14**(7), 2515–2535, ISSN 19940424 (doi: 10.5194/  
513 tc-14-2515-2020)
- 514 Christian JE, Robel AA and Catania G (2022) A probabilistic framework for quantifying the role of anthropogenic  
515 climate change in marine-terminating glacier retreats. *The Cryosphere*, **16**(7), 2725–2743, ISSN 1994-0424 (doi:  
516 10.5194/tc-16-2725-2022)
- 517 Crameri F (2018) Geodynamic diagnostics, scientific visualisation and StagLab 3.0. *Geoscientific Model Development*,  
518 **11**(6), 2541–2562, ISSN 1991-9603 (doi: 10.5194/gmd-11-2541-2018)
- 519 Csatho BM, Schenka AF, Van Der Veen CJ, Babonis G, Duncan K, Rezvanbehbahani S, Van Den Broeke MR,  
520 Simonsen SB, Nagarajan S and Van Angelen JH (2014) Laser altimetry reveals complex pattern of Greenland  
521 Ice Sheet dynamics. *Proceedings of the National Academy of Sciences of the United States of America*, **111**(52),  
522 18478–18483, ISSN 10916490 (doi: 10.1073/pnas.1411680112)
- 523 Cuffey KM and Paterson WSB (2010) *The physics of glaciers*. Elsevier, Oxford, 4th edition, ISBN 9780080919126
- 524 Dawson EJ, Schroeder DM, Chu W, Mantelli E and Seroussi H (2022) Ice mass loss sensitivity to the Antarctic  
525 ice sheet basal thermal state. *Nature Communications* 2022 13:1, **13**(1), 1–9, ISSN 2041-1723 (doi: 10.1038/  
526 s41467-022-32632-2)
- 527 de Fleurian B, Morlighem M, Seroussi H, Rignot E, van den Broeke MR, Kuipers Munneke P, Mouginot J, Smeets  
528 PC and Tedstone AJ (2016) A modeling study of the effect of runoff variability on the effective pressure beneath  
529 Russell Glacier, West Greenland. *Journal of Geophysical Research: Earth Surface*, **121**(10), 1834–1848, ISSN  
530 2169-9011 (doi: 10.1002/2016JF003842)
- 531 Doyle SH, Hubbard A, Fitzpatrick AA, Van As D, Mikkelsen AB, Petterson R and Hubbard B (2014) Persistent flow  
532 acceleration within the interior of the Greenland ice sheet. *Geophysical Research Letters*, **41**(3), 899–905, ISSN  
533 1944-8007 (doi: 10.1002/2013GL058933)

- 534 Dunse T, Schellenberger T, Hagen JO, Kääb A, Schuler TV and Reijmer CH (2015) Glacier-surge mechanisms  
535 promoted by a hydro-thermodynamic feedback to summer melt. *Cryosphere*, **9**(1), 197–215, ISSN 19940424 (doi:  
536 10.5194/TC-9-197-2015)
- 537 Enderlin EM, Howat IM and Vieli A (2013) High sensitivity of tidewater outlet glacier dynamics to shape. *Cryosphere*,  
538 **7**(3), 1007–1015, ISSN 19940416 (doi: 10.5194/TC-7-1007-2013)
- 539 Enderlin EM, Hamilton GS, O’Neel S, Bartholomaus TC, Morlighem M and Holt JW (2016) An Empirical Approach  
540 for Estimating Stress-Coupling Lengths for Marine-Terminating Glaciers. *Frontiers in Earth Science*, **4**, ISSN  
541 2296-6463 (doi: 10.3389/feart.2016.00104)
- 542 Felikson D, Bartholomaus TC, Catania GA, Korsgaard NJ, Kjær KH, Morlighem M, Noël B, Van Den Broeke M,  
543 Stearns LA, Shroyer EL, Sutherland DA and Nash JD (2017) Inland thinning on the Greenland ice sheet controlled  
544 by outlet glacier geometry. *Nature Geoscience*, **10**(5), 366–369, ISSN 17520908 (doi: 10.1038/ngeo2934)
- 545 Felikson D, A Catania G, Bartholomaus TC, Morlighem M and Noël BP (2021) Steep Glacier Bed Knickpoints  
546 Mitigate Inland Thinning in Greenland. *Geophysical Research Letters*, **48**(2), 1–10, ISSN 19448007 (doi: 10.1029/  
547 2020GL090112)
- 548 Felikson D, Nowicki S, Nias I, Morlighem M and Seroussi H (2022) Seasonal Tidewater Glacier Terminus Oscillations  
549 Bias Multi-Decadal Projections of Ice Mass Change. *Journal of Geophysical Research: Earth Surface*, **127**(2),  
550 e2021JF006249, ISSN 2169-9011 (doi: 10.1029/2021JF006249)
- 551 Fox-Kemper B, Hewitt H, Xiao C, Aðalgeirsdóttir G, Drijfhout S, Edwards T, Golledge N, Hemer M, Kopp R, Krinner  
552 G, Mix A, Notz D, Nowicki S, Nurhati I, Ruiz L, Sallée JB, Slangen A and Yu Y (2023) Ocean, Cryosphere and  
553 Sea Level Change. In *Climate Change 2021 – The Physical Science Basis*, 1211–1362, Cambridge University Press  
554 (doi: 10.1017/9781009157896.011)
- 555 Frank T, Åkesson H, De Fleurian B, Morlighem M and Nisancioglu KH (2022) Geometric controls of tidewater glacier  
556 dynamics. *Cryosphere*, **16**(2), 581–601, ISSN 19940424 (doi: 10.5194/TC-16-581-2022)
- 557 Gladstone RM, Lee V, Vieli A and Payne AJ (2010) Grounding line migration in an adaptive mesh ice sheet model.  
558 *Journal of Geophysical Research: Earth Surface*, **115**(F4), 4014, ISSN 2156-2202 (doi: 10.1029/2009JF001615)
- 559 Goelzer H, Nowicki S, Edwards T, Beckley M, Abe-Ouchi A, Aschwanden A, Calov R, Gagliardini O, Gillet-Chaulet F,  
560 Golledge NR, Gregory J, Greve R, Humbert A, Huybrechts P, Kennedy JH, Larour E, Lipscomb WH, Leclech S, Lee  
561 V, Morlighem M, Pattyn F, Payne AJ, Rodehacke C, Rückamp M, Saito F, Schlegel N, Seroussi H, Shepherd A, Sun  
562 S, Van De Wal R and Ziemann FA (2018) Design and results of the ice sheet model initialisation initMIP-Greenland:  
563 An ISMIP6 intercomparison. *Cryosphere*, **12**(4), 1433–1460, ISSN 19940424 (doi: 10.5194/tc-12-1433-2018)

- 564 Goelzer H, Nowicki S, Payne A, Larour E, Seroussi H, Lipscomb WH, Gregory J, Abe-Ouchi A, Shepherd A, Simon  
565 E, Agosta C, Alexander P, Aschwanden A, Barthel A, Calov R, Chambers C, Choi Y, Cuzzone J, Dumas C,  
566 Edwards T, Felikson D, Fettweis X, Golledge NR, Greve R, Humbert A, Huybrechts P, Le Clec'H S, Lee V,  
567 Leguy G, Little C, Lowry D, Morlighem M, Nias I, Quiquet A, Rückamp M, Schlegel NJ, Slater DA, Smith R,  
568 Straneo F, Tarasov L, Van De Wal R and Van Den Broeke M (2020) The future sea-level contribution of the  
569 Greenland ice sheet: A multi-model ensemble study of ISMIP6. *Cryosphere*, **14**(9), 3071–3096, ISSN 19940424  
570 (doi: 10.5194/TC-14-3071-2020)
- 571 Goliber S, Black T, Catania G, Lea JM, Olsen H, Cheng D, Bevan S, Bjørk A, Bunce C, Brough S, Carr JR, Cowton  
572 T, Gardner A, Fahrner D, Hill E, Joughin I, Korsgaard NJ, Luckman A, Moon T, Murray T, Sole A, Wood M  
573 and Zhang E (2022) TermPicks: a century of Greenland glacier terminus data for use in scientific and machine  
574 learning applications. *Cryosphere*, **16**(8), 3215–3233, ISSN 19940424 (doi: 10.5194/TC-16-3215-2022)
- 575 Gong Y, Zwinger T, Åström J, Altena B, Schellenberger T, Gladstone R and Moore JC (2018) Simulating the  
576 roles of crevasse routing of surface water and basal friction on the surge evolution of Basin 3, Austfonna ice cap.  
577 *Cryosphere*, **12**(5), 1563–1577, ISSN 19940424 (doi: 10.5194/TC-12-1563-2018)
- 578 Greene CA, Thirumalai K, Kearney KA, Delgado JM, Schwanghart W, Wolfenbarger NS, Thyng KM, Gwyther DE,  
579 Gardner AS and Blankenship DD (2019) The Climate Data Toolbox for MATLAB. *Geochemistry, Geophysics,*  
580 *Geosystems*, **20**(7), 3774–3781, ISSN 1525-2027 (doi: 10.1029/2019GC008392)
- 581 Gudmundsson GH (2003) Transmission of basal variability to a glacier surface. *Journal of Geophysical Research:*  
582 *Solid Earth*, **108**(B5), 1–19, ISSN 2169-9356 (doi: 10.1029/2002jb002107)
- 583 Habermann M, Truffer M and Maxwell D (2013) Changing basal conditions during the speed-up of Jakobshavn Isbræ,  
584 Greenland. *Cryosphere*, **7**(6), 1679–1692, ISSN 19940424 (doi: 10.5194/TC-7-1679-2013)
- 585 Haseloff M and Sergienko OV (2018) The effect of buttressing on grounding line dynamics. *Journal of Glaciology*,  
586 **64**(245), 417–431, ISSN 0022-1430 (doi: 10.1017/JOG.2018.30)
- 587 Hill EA, Rachel Carr J, Stokes CR and Hilmar Gudmundsson G (2018) Dynamic changes in outlet glaciers in northern  
588 Greenland from 1948 to 2015. *Cryosphere*, **12**(10), 3243–3263, ISSN 19940424 (doi: 10.5194/TC-12-3243-2018)
- 589 Jordan TM, Cooper MA, Schroeder DM, Williams CN, Paden JD, Siegert MJ and Bamber JL (2017) Self-affine  
590 subglacial roughness: consequences for radar scattering and basal water discrimination in northern Greenland.  
591 *The Cryosphere*, **11**(3), 1247–1264, ISSN 1994-0424 (doi: 10.5194/tc-11-1247-2017)
- 592 Joughin I, Smith BE and Schoof CG (2019) Regularized Coulomb Friction Laws for Ice Sheet Sliding: Application to  
593 Pine Island Glacier, Antarctica. *Geophysical Research Letters*, **46**(9), 4764–4771, ISSN 1944-8007 (doi: 10.1029/  
594 2019GL082526)



- 595 Kamb B and Echelmeyer KA (1986) Stress-Gradient Coupling in Glacier Flow: I. Longitudinal Averaging of the  
596 Influence of Ice Thickness and Surface Slope. *Journal of Glaciology*, **32**(111), 267–284, ISSN 0022-1430 (doi:  
597 10.3189/S0022143000015604)
- 598 Kehrl LM, Joughin I, Shean DE, Floricioiu D and Krieger L (2017) Seasonal and interannual variabilities in terminus  
599 position, glacier velocity, and surface elevation at Helheim and Kangerlussuaq Glaciers from 2008 to 2016. *Journal*  
600 *of Geophysical Research: Earth Surface*, **122**(9), 1635–1652, ISSN 2169-9011 (doi: 10.1002/2016JF004133)
- 601 Khazendar A, Fenty IG, Carroll D, Gardner A, Lee CM, Fukumori I, Wang O, Zhang H, Seroussi H, Moller D,  
602 Noël BP, van den Broeke MR, Dinardo S and Willis J (2019) Interruption of two decades of Jakobshavn Isbrae  
603 acceleration and thinning as regional ocean cools. *Nature Geoscience 2019 12:4*, **12**(4), 277–283, ISSN 1752-0908  
604 (doi: 10.1038/s41561-019-0329-3)
- 605 Larour E, Seroussi H, Morlighem M and Rignot E (2012) Continental scale, high order, high spatial resolution, ice  
606 sheet modeling using the Ice Sheet System Model (ISSM). *Journal of Geophysical Research: Earth Surface*, **117**(1),  
607 ISSN 21699011 (doi: 10.1029/2011JF002140)
- 608 McFadden EM, Howat IM, Joughin I, Smith BE and Ahn Y (2011) Changes in the dynamics of marine terminating  
609 outlet glaciers in west Greenland (2000-2009). *Journal of Geophysical Research: Earth Surface*, **116**(2), 1–16, ISSN  
610 21699011 (doi: 10.1029/2010JF001757)
- 611 Mona Mahboob Kanafi (2023) Surface generator: artificial randomly rough surfaces
- 612 Moon T, Joughin I, Smith B, Van Den Broeke MR, Van De Berg WJ, Noël B and Usher M (2014) Distinct patterns  
613 of seasonal Greenland glacier velocity. *Geophysical Research Letters*, **41**(20), 7209–7216, ISSN 19448007 (doi:  
614 10.1002/2014GL061836)
- 615 Moon TA, Gardner AS, Csatho B, Parmuzin I and Fahnestock MA (2020) Rapid Reconfiguration of the Greenland  
616 Ice Sheet Coastal Margin. *Journal of Geophysical Research: Earth Surface*, **125**(11), ISSN 21699011 (doi: 10.  
617 1029/2020JF005585)
- 618 Mouginit J, Rignot E, Bjørk AA, van den Broeke M, Millan R, Morlighem M, Noël B, Scheuchl B and Wood M (2019)  
619 Forty-six years of Greenland Ice Sheet mass balance from 1972 to 2018. *Proceedings of the National Academy of*  
620 *Sciences of the United States of America*, **116**(19), 9239–9244, ISSN 10916490 (doi: 10.1073/PNAS.1904242116/  
621 SUPPL{\\_}FILE/PNAS.1904242116.SD02.XLSX)
- 622 Nick FM, Vieli A, Howat IM and Joughin I (2009) Large-scale changes in Greenland outlet glacier dynamics triggered  
623 at the terminus. *Nature Geoscience 2009 2:2*, **2**(2), 110–114, ISSN 1752-0908 (doi: 10.1038/ngeo394)

- 624 Pfeffer WT (2007) A simple mechanism for irreversible tidewater glacier retreat. *Journal of Geophysical Research: Earth Surface*, **112**(F3), 3–25, ISSN 2156-2202 (doi: 10.1029/2006JF000590)
- 625
- 626 Poinar K, Dow CF and Andrews LC (2019) Long-Term Support of an Active Subglacial Hydrologic System in Southeast Greenland by Firn Aquifers. *Geophysical Research Letters*, **46**(9), 4772–4781, ISSN 1944-8007 (doi: 10.1029/2019GL082786)
- 627
- 628
- 629 Pritchard HD, Arthern RJ, Vaughan DG and Edwards LA (2009) Extensive dynamic thinning on the margins of the Greenland and Antarctic ice sheets. *Nature* 2009 461:7266, **461**(7266), 971–975, ISSN 1476-4687 (doi: 10.1038/nature08471)
- 630
- 631
- 632 Robel AA (2017) Thinning sea ice weakens buttressing force of iceberg mélange and promotes calving. *Nature Communications* 2017 8:1, **8**(1), 1–7, ISSN 2041-1723 (doi: 10.1038/ncomms14596)
- 633
- 634 Schenk T and Csathó B (2012) A new methodology for detecting ice sheet surface elevation changes from laser altimetry data. *IEEE Transactions on Geoscience and Remote Sensing*, **50**(9), 3302–3316, ISSN 01962892 (doi: 10.1109/TGRS.2011.2182357)
- 635
- 636
- 637 Schoof C (2005) The effect of cavitation on glacier sliding. *Proceedings of the Royal Society A: Mathematical, Physical and Engineering Sciences*, **461**(2055), 609–627, ISSN 14712946 (doi: 10.1098/RSPA.2004.1350)
- 638
- 639 Schoof C (2007) Ice sheet grounding line dynamics: Steady states, stability, and hysteresis. *Journal of Geophysical Research: Earth Surface*, **112**(3), ISSN 21699011 (doi: 10.1029/2006JF000664)
- 640
- 641 Schoof C (2010) Ice-sheet acceleration driven by melt supply variability. *Nature*, **468**(7325), 803–806, ISSN 0028-0836 (doi: 10.1038/nature09618)
- 642
- 643 Sergienko OV (2013) Glaciological twins: basally controlled subglacial and supraglacial lakes. *Journal of Glaciology*, **59**(213), 3–8, ISSN 0022-1430 (doi: 10.3189/2013JoG12J040)
- 644
- 645 Sergienko OV and Hulbe CL (2011) ‘Sticky spots’ and subglacial lakes under ice streams of the Siple Coast, Antarctica. *Annals of Glaciology*, **52**(58), 18–22, ISSN 0260-3055 (doi: 10.3189/172756411797252176)
- 646
- 647 Slater DA, Nienow PW, Goldberg DN, Cowton TR and Sole AJ (2017) A model for tidewater glacier undercutting by submarine melting. *Geophysical Research Letters*, **44**(5), 2360–2368, ISSN 19448007 (doi: 10.1002/2016GL072374)
- 648
- 649 Slater DA, Straneo F, Felikson D, Little CM, Goelzer H, Fettweis X and Holte J (2019) Estimating Greenland tidewater glacier retreat driven by submarine melting. *Cryosphere*, **13**(9), 2489–2509, ISSN 19940424 (doi: 10.5194/TC-13-2489-2019)
- 650
- 651

- 652 Slater DA, Felikson D, Straneo F, Goelzer H, Little CM, Morlighem M, Fettweis X and Nowicki S (2020) Twenty-  
653 first century ocean forcing of the Greenland ice sheet for modelling of sea level contribution. *Cryosphere*, **14**(3),  
654 985–1008, ISSN 19940424 (doi: 10.5194/tc-14-985-2020)
- 655 Sommers A, Meyer C, Morlighem M, Rajaram H, Poinar K, Chu W and Mejia J (2023) Subglacial hydrology modeling  
656 predicts high winter water pressure and spatially variable transmissivity at Helheim Glacier, Greenland. *Journal*  
657 *of Glaciology*, 1–13, ISSN 0022-1430 (doi: 10.1017/JOG.2023.39)
- 658 Steiger N, Nisancioglu KH, Åkesson H, De Fleurian B and Nick FM (2018) Simulated retreat of Jakobshavn Isbræ  
659 since the Little Ice Age controlled by geometry. *Cryosphere*, **12**(7), 2249–2266, ISSN 19940424 (doi: 10.5194/  
660 tc-12-2249-2018)
- 661 Stevens LA, Nettles M, Davis JL, Creyts TT, Kingslake J, Hewitt IJ and Stubblefield A (2022) Tidewater-glacier  
662 response to supraglacial lake drainage. *Nature Communications* 2022 13:1, **13**(1), 1–11, ISSN 2041-1723 (doi:  
663 10.1038/s41467-022-33763-2)
- 664 Thomas R, Frederick E, Krabill W, Manizade S and Martin C (2009) Recent changes on Greenland outlet glaciers.  
665 *Journal of Glaciology*, **55**(189), 147–162, ISSN 0022-1430 (doi: 10.3189/002214309788608958)
- 666 Tsai VC, Stewart AL and Thompson AF (2015) Marine ice-sheet profiles and stability under Coulomb basal condi-  
667 tions. *Journal of Glaciology*, **61**(226), 205–215, ISSN 0022-1430 (doi: 10.3189/2015JOG14J221)
- 668 van de Wal RS and Oerlemans J (1995) Response of valley glaciers to climate change and kinematic waves: a  
669 study with a numerical ice-flow model. *Journal of Glaciology*, **41**(137), 142–152, ISSN 00221430 (doi: 10.1017/  
670 S0022143000017834)
- 671 van de Wal RS, Boot W, Van Den Broeke MR, Smeets CJ, Reijmer CH, Donker JJ and Oerlemans J (2008) Large  
672 and rapid melt-induced velocity changes in the ablation zone of the Greenland Ice Sheet. *Science*, **321**(5885), 111–  
673 113, ISSN 00368075 (doi: 10.1126/SCIENCE.1158540/ASSET/C7BCE4DB-A082-40AB-802F-FD4D762AFE62/  
674 ASSETS/GRAPHIC/321{\\_}111{\\_}F3.JPEG)
- 675 van der Veen CJ (2001) Greenland ice sheet response to external forcing. *Journal of Geophysical Research Atmo-*  
676 *spheres*, **106**(D24), 34047–34058, ISSN 01480227 (doi: 10.1029/2001JD900032)
- 677 van der Veen CJ and Whillans IM (1989) Force Budget: I. Theory and Numerical Methods. *Journal of Glaciology*,  
678 **35**(119), 53–60, ISSN 0022-1430 (doi: 10.3189/002214389793701581)
- 679 Vijay S, King MD, Howat IM, Solgaard AM, Khan SA and Noël B (2021) Greenland ice-sheet wide glacier classi-  
680 fication based on two distinct seasonal ice velocity behaviors. *Journal of Glaciology*, **67**(266), 1241–1248, ISSN  
681 0022-1430 (doi: 10.1017/JOG.2021.89)

- 682 Wang W, Li J and Zwally HJ (2012) Dynamic inland propagation of thinning due to ice loss at the margins of the  
683 Greenland ice sheet. *Journal of Glaciology*, **58**(210), 734–740, ISSN 00221430 (doi: 10.3189/2012JoG11J187)
- 684 Weertman J (1957) On the Sliding of Glaciers. *Journal of Glaciology*, **3**(21), 33–38, ISSN 0022-1430 (doi: 10.3189/  
685 S0022143000024709)
- 686 Wood M, Rignot E, Fenty I, An L, Bjørk A, van den Broeke M, Cai C, Kane E, Menemenlis D, Millan R, Morlighem  
687 M, Mouginot J, Noël B, Scheuchl B, Velicogna I, Willis JK and Zhang H (2021) Ocean forcing drives glacier retreat  
688 in Greenland. *Science Advances*, **7**(1), 1–11, ISSN 23752548 (doi: 10.1126/sciadv.aba7282)
- 689 Zheng W (2022) Glacier geometry and flow speed determine how Arctic marine-terminating glaciers respond to  
690 lubricated beds. *Cryosphere*, **16**(4), 1431–1445, ISSN 19940424 (doi: 10.5194/TC-16-1431-2022)

691 **A APPENDIX A: SUPPLEMENTARY TABLES**

Synthetic testbeds geometry at steady state			
Name	Width (m)	Depth (effective depth) (m)	Floating termini length (km)
W1GL0FC1	4000	-100 (-142)	0
W1GL1FC1	4000	-500 (-474)	4.717
W1GL0FC2	4000	-100 (-142)	0
W1GL1FC2	4000	-500 (-487)	3.985
W1GL0FC3	4000	-100 (-139)	0
W1GL1FC3	4000	-500 (-488)	4.159
W2GL0FC1	6000	-100 (-157)	0
W2GL1FC1	6000	-500 (-458)	8.446
W2GL0FC2	6000	-100 (-158)	0
W2GL1FC2	6000	-500 (-464)	7.878
W2GL0FC3	6000	-100 (-156)	0
W2GL1FC3	6000	-500 (-467)	7.749
W3GL0FC1	8000	-100 (-162)	0
W3GL1FC1	8000	-500 (-425)	11.543
W3GL0FC2	8000	-100 (-164)	0
W3GL1FC2	8000	-500 (-426)	11.421
W3GL0FC3	8000	-100 (-162)	0
W3GL1FC3	8000	-500 (-428)	11.256

**Table 2.** Characteristics of the synthetic testbeds at their steady state. The nomenclature of the testbed names: “W” stands for fjord width, “GL” stands for grounding line depth, and “FC” stands for the sliding law coefficient. Numbers that follow: 1 to 3 represents low to high values; 0 and 1 respectively represents the testbed glaciers with shallow and with deep grounding lines. “Depth” is the grounding line depth at the start of the model run, and “effective depth” means grounding line depth after the model relaxation.

Kinematic characteristics of synthetic testbeds at steady state									
Name	Velocity (m a <sup>-1</sup> )			Thickness (m)			Basal drag (kPa)		
	min	mean	max	min	mean	max	min	mean	max
W1GL0FC1	2585	3470	4898	111	303	389	16	27	57
W1GL1FC1	1530	2168	2333	342	545	572	8	18	42
W1GL0FC2	1164	1684	2702	117	340	451	35	49	84
W1GL1FC2	814	1087	1246	327	555	599	16	33	63
W1GL0FC3	571	865	1619	125	402	544	82	94	127
W1GL1FC3	526	653	806	302	554	633	41	74	101
W2GL0FC1	2448	3306	4162	131	279	331	13	23	30
W2GL1FC1	1478	2184	2357	294	503	519	8	15	25
W2GL0FC2	1050	1418	1963	133	303	374	25	38	45
W2GL1FC2	674	942	1096	272	496	528	14	26	38
W2GL0FC3	481	689	1098	138	356	458	51	73	85
W2GL1FC3	399	521	650	241	476	542	33	57	71
W3GL0FC1	2102	3131	3765	134	265	306	10	21	26
W3GL1FC1	1352	2180	2349	253	461	480	7	15	21
W3GL0FC2	872	1228	1588	133	281	337	17	33	39
W3GL1FC2	568	867	1004	224	437	479	11	24	31
W3GL0FC3	416	575	844	135	326	412	36	61	68
W3GL1FC3	332	485	587	194	398	471	26	52	65

**Table 3.** Kinematic characteristics of the synthetic testbeds at their steady state. Testbed nomenclature is the same as in Table 2. The statistics of velocity, thickness, and basal drag are calculated based on the data from the first 10 km behind the grounding line.

Maximum $\Delta H$ and $dH/dt$ in the localized basal perturbation experiment				
Name	Diffused pulse		Transient pulse	
	max $\Delta H$ (m)	max $dH/dt$ (m a <sup>-1</sup> )	max $\Delta H$ (m)	max $dH/dt$ (m a <sup>-1</sup> )
W1GL0FC1	4.87	4.91	3.63	21.81
W1GL1FC1	7.48	6.79	5.93	30.81
W1GL0FC2	5.31	5.38	3.67	20.34
W1GL1FC2	9.35	9.06	7.58	41.39
W1GL0FC3	5.58	5.02	3.47	18.46
W1GL1FC3	10.76	10.57	8.56	45.88
W2GL0FC1	5.69	5.48	3.86	22.08
W2GL1FC1	9.29	8.48	6.78	32.32
W2GL0FC2	5.82	5.24	3.56	18.67
W2GL1FC2	9.91	9.89	7.73	40.16
W2GL0FC3	5.88	4.44	3.26	15.78
W2GL1FC3	10.73	10.48	8.05	41.86
W3GL0FC1	6.29	5.93	4.05	22.59
W3GL1FC1	10.29	11.24	7.00	32.43
W3GL0FC2	5.98	4.93	3.44	17.39
W3GL1FC2	7.91	8.60	5.89	31.61
W3GL0FC3	5.86	3.96	3.10	13.49
W3GL1FC3	8.68	8.17	6.11	32.44

**Table 4.** Max elevation change and change rate in localized basal perturbation experiments. Testbed nomenclature is the same as shown in table 2.

Max thinning rate (m a <sup>-1</sup> )	Shallow testbeds			Deep testbeds			
	Mean basal shear stress						
		Low	Medium	High	Low	Medium	High
Fjord width	Narrow	5.0	5.5	6.2	10.4	12.0	16.0
	Medium	4.1	4.5	5.3	10.4	10.1	12.5
	Wide	3.7	4.0	4.7	10.5	8.4	9.4

**Table 5.** Max thinning rate from overburden pressure experiment, accompanying Fig. 3

Attenuation distance (m)	Shallow testbeds			Deep testbeds			
	Mean basal shear stress						
	Low	Medium	High	Low	Medium	High	
Fjord width	Narrow	30987.9	25321.2	19832.0	32815.4	28199.6	22736.5
	Medium	30640.2	24510.5	19270.5	33632.2	28881.5	23824.0
	Wide	30397.2	23798.9	18680.9	33829.0	29011.3	24358.1

**Table 6.** Attenuation distance of diffusive thinning from overburden pressure experiment.

## 692 B APPENDIX B: SUPPLEMENTARY METHOD

### 693 B.1 Ice dynamics simulation

694 We use the MATLAB version of Ice-sheet and Sea-level System Model (ISSM version 4.21) to simulate ice  
 695 flow dynamics. In the following sections, the definitions of variables can be found in Table 1 in the main  
 696 text.

### 697 B.2 Synthetic testbed

For all testbeds, we applied a linear surface mass balance relationship:

$$\text{SMB}(x) = 0.5\left(1 - \frac{2}{L_x}x\right) \quad (\text{B.4})$$

698 where  $x$  is the distance from the influx boundary and  $L_x$  is the along-flow domain length. This fixes the  
 699 equilibrium line altitude at  $x = L_x/2$ .

The across-flow bed topography was prescribed similarly to Felikson and others (2022)

$$B_y(y) = \frac{d_c}{1 + e^{-2/f_c(y-L_y/2-w_c(x))}} + \frac{d_c}{1 + e^{-2/f_c(y-L_y/2+w_c(x))}} \quad (\text{B.5})$$

700 where  $y$  is across-flow direction,  $L_y$  is model domain width,  $f_c$  is the characteristic width of channel side  
 701 walls, and  $d_c$  defines the depth of the trough compared to the top of side walls.

In our base experiments, we did not allow bed topography undulation for our base experiments and



therefore prescribed the along-flow bedrock depth as a linear function:

$$B_x(x) = B_0 + \left( \frac{B_{gl} - B_0}{L_x} \right) x \quad (\text{B.6})$$

where  $B_0$  is the bed depth at the influx boundary and  $B_{gl}$  is the grounding line depth, and the bed slopes toward the ocean (prograde) to mitigate any potential run-away retreat. The width of the trough  $w_c(x)$  narrows along the flow. It has a funnel shape that starts with a fixed width (across all testbeds) at the inflow boundary and narrows for the first  $x_f = 15$  km and reaches a constant width throughout the rest of the flow trunk. We parameterized the narrowing stage as with a parabolic function:

$$w_c(x) = \begin{cases} \left[ \left( \frac{L_y/W - 1}{x_f^2} \right) (x - x_f)^2 + 1 \right] W & 0 \leq x \leq x_f \\ W & x \geq x_f \end{cases} \quad (\text{B.7})$$

The prescribed Weertman sliding law coefficient  $C_w$  for model initialization is spatially variable. Its lateral variability is prescribed to be similar to the bed topography while its along-flow variation is conditioned to decay exponentially toward the calving front:

$$C_w(x, y) = \frac{C_{wo}(3 - e)e^{-2(x/L_x)}}{1 + e^{-2/f_c(y - L_y/2 - w_c(x))}} + \frac{C_{wo}(3 - e)e^{-2(x/L_x)}}{1 + e^{2/f_c(y - L_y/2 + w_c(x))}} \quad (\text{B.8})$$

702 The numerator helps define the e-folding length over which the sliding law coefficient decreases toward the  
703 terminus. This serves to regulate the ice velocity near the influx boundary and alleviate solver convergence  
704 issue when the prescribed sliding law coefficient law is low.

705 To initialize the model, we used the plastic ice sheet profile as an initial guess of glacier thickness,  
706 assuming an ice tensile strength of 1 MPa. At the influx boundary, we fixed the ice thickness as defined by  
707 the initial profile and imposed a constant 100 meter per year along-flow ice velocity. Since the flow domain  
708 length remains constant across all testbeds, the ice thickness at the inflow boundary and hence the flux  
709 are also identical across all testbeds.

710 During the initialization, the transient simulations have an adaptive time step based on Courant–Friedrichs–Lewy  
711 condition. During subsequent “control” and “overburden pressure experiment” runs, the time steps are  
712 fixed at 0.1 year. During the localized basal perturbation runs, the time steps are fixed at 0.01 year,  
713 although we only record the simulation output every 0.1 year.

### 714 B.3 Experiment design

#### 715 B.3.1 Control

After the testbed was initialized to its steady state, we forced the calving front to retreat at a rate characterized by a triangular function:

$$\nu(t) = \begin{cases} \frac{\nu_m t_s}{t_s - t_e} + \frac{\nu_m}{t_e - t_s} t & t_s < t \leq (t_s + t_e)/2 \\ \frac{\nu_m t_e}{t_e - t_s} - \frac{\nu_m}{t_e - t_s} t & (t_s + t_e)/2 < t \leq t_e \\ 0 & \text{otherwise} \end{cases} \quad (\text{B.9})$$

716 where we defined  $\nu_m$  as the maximum retreat rate, and  $t_s$  and  $t_e$  the start and end year of calving front  
717 perturbation.

#### 718 B.3.2 Localized basal perturbation

While the overburden pressure experiment accounts for changes in ice overburden pressure from ice thickness change, a localized reduction of basal drag represents basal lubrication due to melt water. Mathematically, we wrote the sliding law coefficients as

$$C_{bp} = C_b + \Delta C(x, y, t; \hat{w}) \quad (\text{B.10})$$

where  $C_{bp}$  is the sliding law coefficient for localized basal perturbation,  $C_b$  the sliding law coefficient for overburden pressure experiment (Budd sliding), and  $\Delta C(x, y, t; w)$  is determined by either of the two pulses:

$$\Delta C(x, y, t; \hat{w})_{\text{TP}} = \hat{C} \exp \left[ -3 \left( \frac{t}{t_p} \right)^2 \right] \exp \left[ -\frac{(x - x_0)^2}{2\hat{w}^2} - \frac{(y - W/2)^2}{2\hat{w}^2} \right] \quad (\text{B.11})$$

$$\Delta C(x, y, t; \hat{w})_{\text{DP}} = \hat{C} \left( \frac{t_p}{t_d} \right) \exp \left[ -3 \left( \frac{t}{t_d} \right)^2 \right] \exp \left[ -\frac{(x - x_0)^2}{2\hat{w}^2} - \frac{(y - W/2)^2}{2\hat{w}^2} \right] \quad (\text{B.12})$$

Here  $\hat{C}$  and  $\hat{w}$  are scaled sliding law coefficient and localized basal perturbation patch width (one standard deviation), defined as

$$\hat{C} = \phi C_w \quad (\text{B.13})$$

$$\hat{w} = \kappa W \sqrt{\frac{W}{\max(W)}} \quad (\text{B.14})$$

where  $t_p$  and  $t_d$  are respectively the characteristic timescale of Transient Pulse and Diffused Pulse, and  $\max(W)$  is the largest fjord width we construct. In other words,  $\hat{C}$  denotes a proportional reduction of sliding law coefficient at the initial state defined in equation B.8,  $\hat{w}$  denotes a quadratic scaling relation between the fjord width and the perturbation patch width, which is a consequence of the requirement that the fractional area being perturbed in each glacier remains identical across the testbeds, i.e.,  $(\int \Delta C(x, y; W_1) dx dy) / (\int_A dx dy) = (\int \Delta C(x, y; W_2) dx dy) / (\int_A dx dy)$  in which  $W_1$  and  $W_2$  represent two different fjord widths, and  $A$  is an arbitrarily chosen flow area that fully encloses the perturbation.

We formulate the parameterization ensuring that total changes in the two sliding law coefficient are the same in each perturbation cycle:  $\int \Delta C_{TP}(t) dt = \int \Delta C_{DP}(t) dt$ , as stated in the method section. At the end of each perturbation cycle, the perturbation in the sliding law coefficient  $\Delta C$  returns to near-zero level ( $\Delta C < 10^{-4} \text{ kg m}^{-2} \text{ s}^{-1}$ ). Moreover, we previously mentioned that we scaled the magnitude of the sliding law coefficient reduction linearly with respect to the coefficient at the initial state, denoted by  $\phi C_w$ . This decision was made due to a lack of knowledge regarding any general relationship between basal lubrication and various hydrological and glacier geometric factors.

It should be noted that since  $\Delta C_{TP}$  and  $\Delta C_{DP}$  depend on the initial sliding law coefficient  $C_w$ , combining the reductions in the sliding law coefficient from both localized basal perturbation and overburden pressure may result in  $C_{bp}$  dropping below zero as the simulation progresses. In such case, we force the local sliding law coefficient to a minimum of 0 until it rebounds as the localized basal perturbation recovers.

#### B.4 Stress balance

The stress balance states that the gravitational driving stress of a glacier is approximately in balance with the sum of the basal shear stress and the longitudinal and lateral resistive stress gradients:

$$\tau_d \approx \tau_b + \frac{\partial}{\partial x} (HR_{xx}) + \frac{\partial}{\partial y} (HR_{xy}) \quad (\text{B.15})$$

The longitudinal resistive stress  $R_{xx}$  and the lateral resistive stress  $R_{xy}$  can be calculated respectively as

$$R_{xx} = B \dot{\epsilon}_e^{1/n-1} (2\dot{\epsilon}_{xx} + \dot{\epsilon}_{yy}) \quad (\text{B.16})$$

$$R_{xy} = B \dot{\epsilon}_e^{1/n-1} \dot{\epsilon}_{xy} \quad (\text{B.17})$$

where  $B$  is ice rigidity;  $\dot{\epsilon}_{xx}$ ,  $\dot{\epsilon}_{xy}$ , and  $\dot{\epsilon}_{yy}$  are strain rates in the subscripted directions, and  $\dot{\epsilon}_e$  is the effective strain rate, defined here as its second tensor invariant, as is commonly done:

$$\dot{\epsilon}_e = (\dot{\epsilon}_{xx}^2 + \dot{\epsilon}_{xy}^2 + \dot{\epsilon}_{yy}^2 + \dot{\epsilon}_{xx}\dot{\epsilon}_{yy})^{1/2} \quad (\text{B.18})$$

738 We applied a five-point finite difference stencil to calculate spatial derivatives and then smoothed the  
 739 derived stress components using a Gaussian filter with a 2 km standard deviation, which we chose to be  
 740 approximately 5–7 times the ice thickness, following Frank and others (2022). The smoothing has a dual  
 741 purpose: to reduce noise resulting from computing the numerical derivative, and to account for the coupling  
 742 length of the longitudinal stress gradient (Kamb and Echelmeyer, 1986; Enderlin and others, 2016).

To calculate the frontal resistive stress loss  $\Delta R$  (Sect. 2.5), we differenced the frontal resistive stress summed along the glacier from the calving front to the grounding line, between the first and last time steps:

$$\Delta R = \int_0^{t_e} \frac{d}{dt} \left[ \int_{X_g(t)}^{X_c(t)} \left( \tau_b + \frac{\partial}{\partial x} (HR_{xx}) + \frac{\partial}{\partial y} (HR_{xy}) \right) dx \right] dt \quad (\text{B.19})$$

743 where  $X_g$  denotes the location of the grounding line,  $X_c$  the location of the calving front, and  $t_e$  the final  
 744 year of the perturbation. We evaluate the integral numerically with the trapezoidal rule.

## 745 C APPENDIX C: SUPPLEMENTARY FIGURES

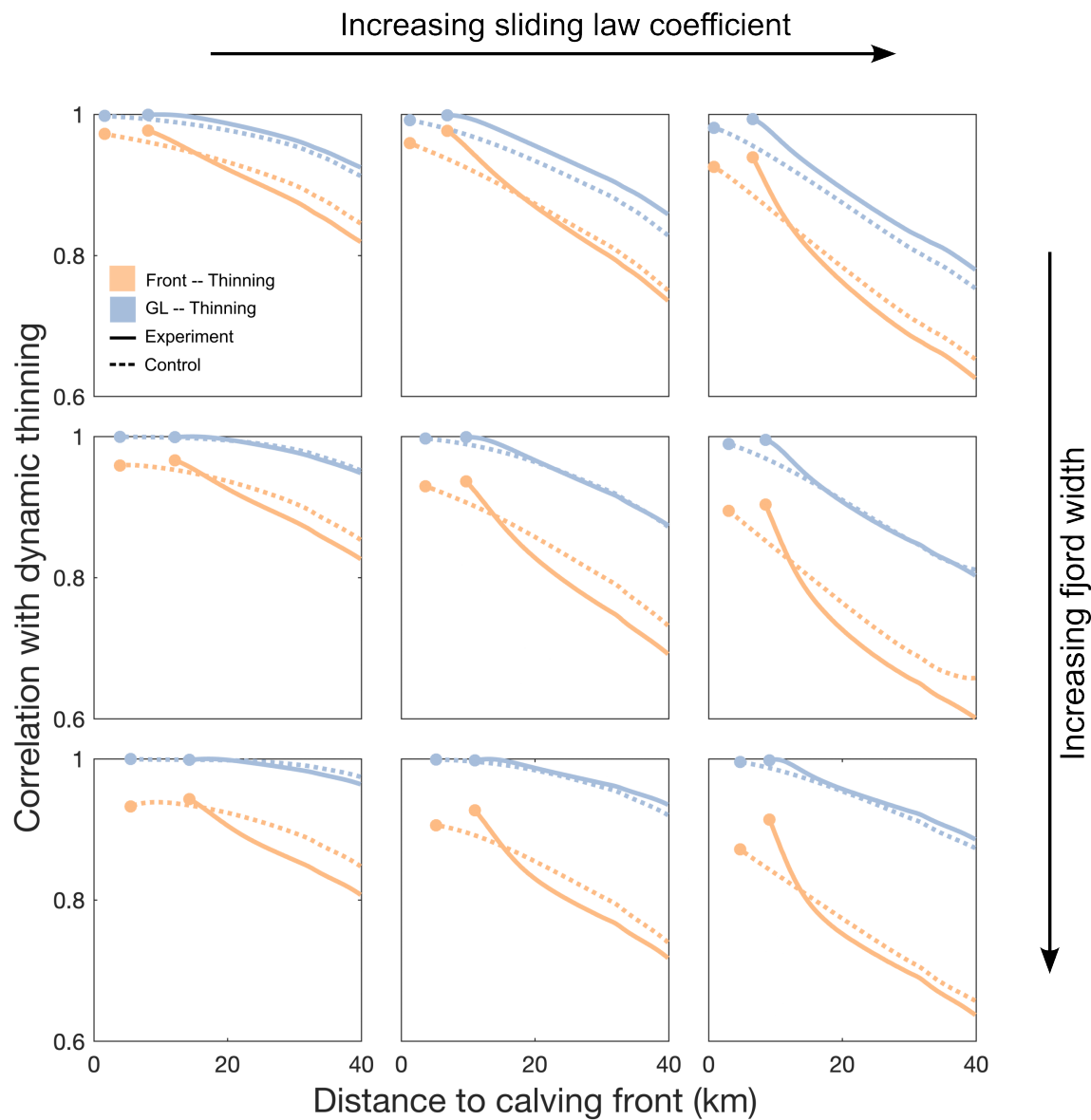


**Fig. 9.** Timeseries correlation between dynamic thinning, grounding line, and frontal retreat. Correlation over the 16-year perturbation between dynamic thinning and the grounding line position (blue), and dynamic thinning and frontal retreat (orange). For a given model run, thinning rates are sampled at every 0.1 year at every 100 meters along the central flowline, plotted here along the x-axis. “GL” denotes grounding line retreat. “Experiment” represents the overburden pressure experiment and “Control” represents the control run. Round markers represent the last position of either the ice front or the grounding line.

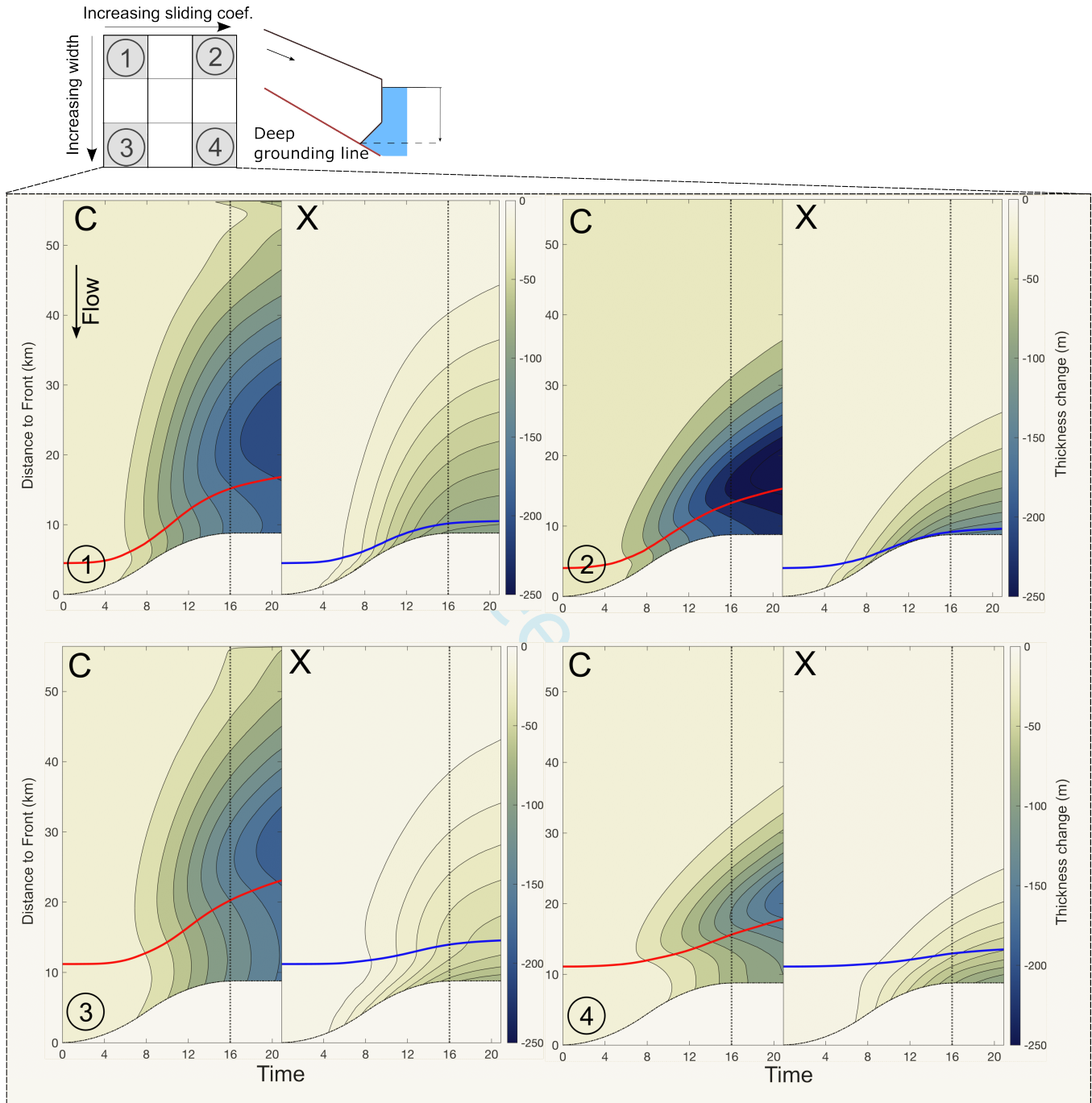


**Fig. 10.** Dynamic thickness change in **deep** testbed glaciers along the center flow line over time, using  $m = 5$  in Budd sliding law, in comparison to  $m = 1$  in the main text (Figure 3). Different from the main text, here we are comparing two simulations both using Budd law but different exponents  $m$  on the sliding velocity. “C” and “X” represent the linear viscous case  $m = 1$  and the more plastic  $m = 5$  case respectively, and the red and blue lines represent the grounding lines in respective cases.

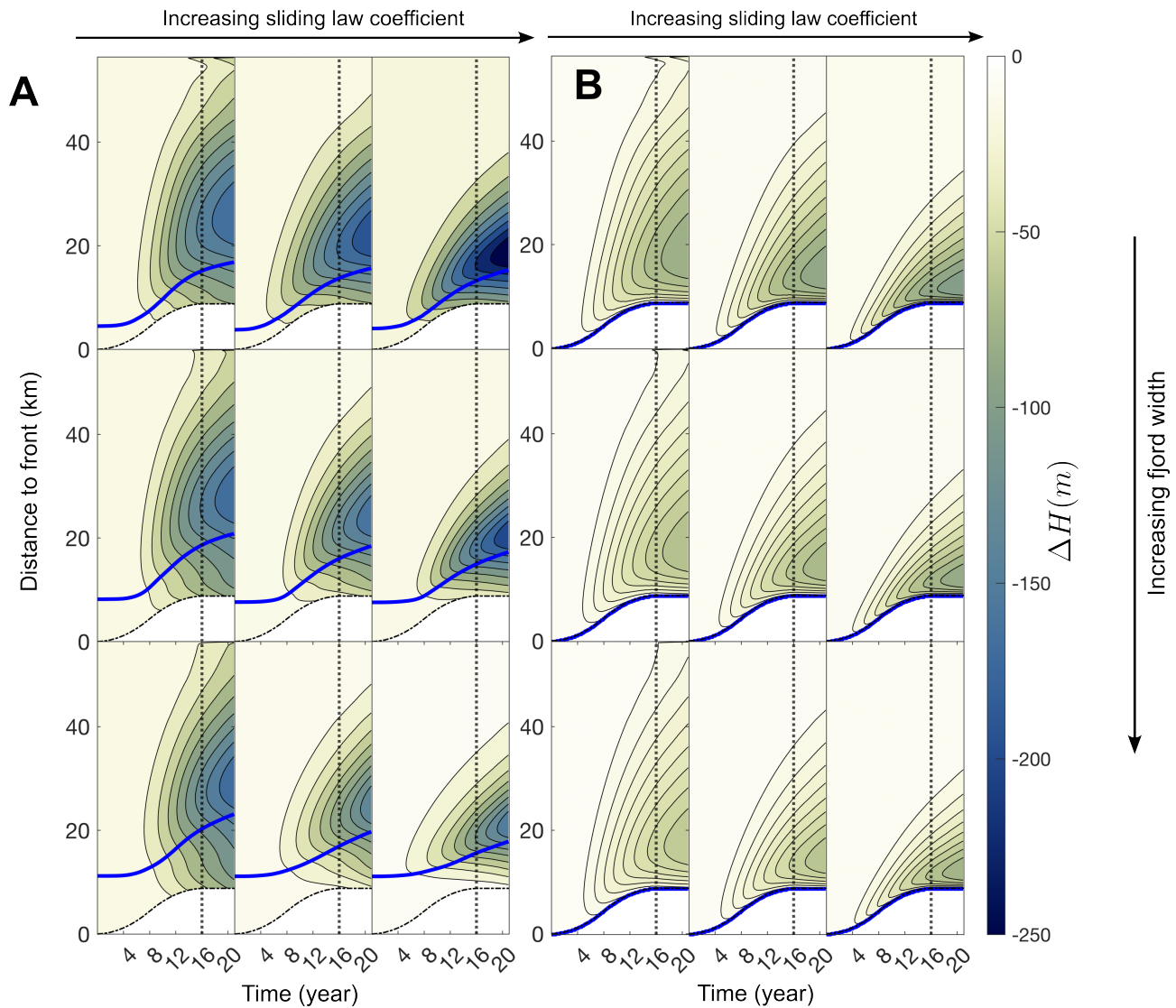


**Fig. 11.** Dynamic thickness change at **deep** and **shallow** testbed glaciers attributed to overburden pressure change in the sliding law, using  $m = 1$ . Blue lines represent the grounding lines. A) deep testbed glaciers. B) shallow testbed glaciers.

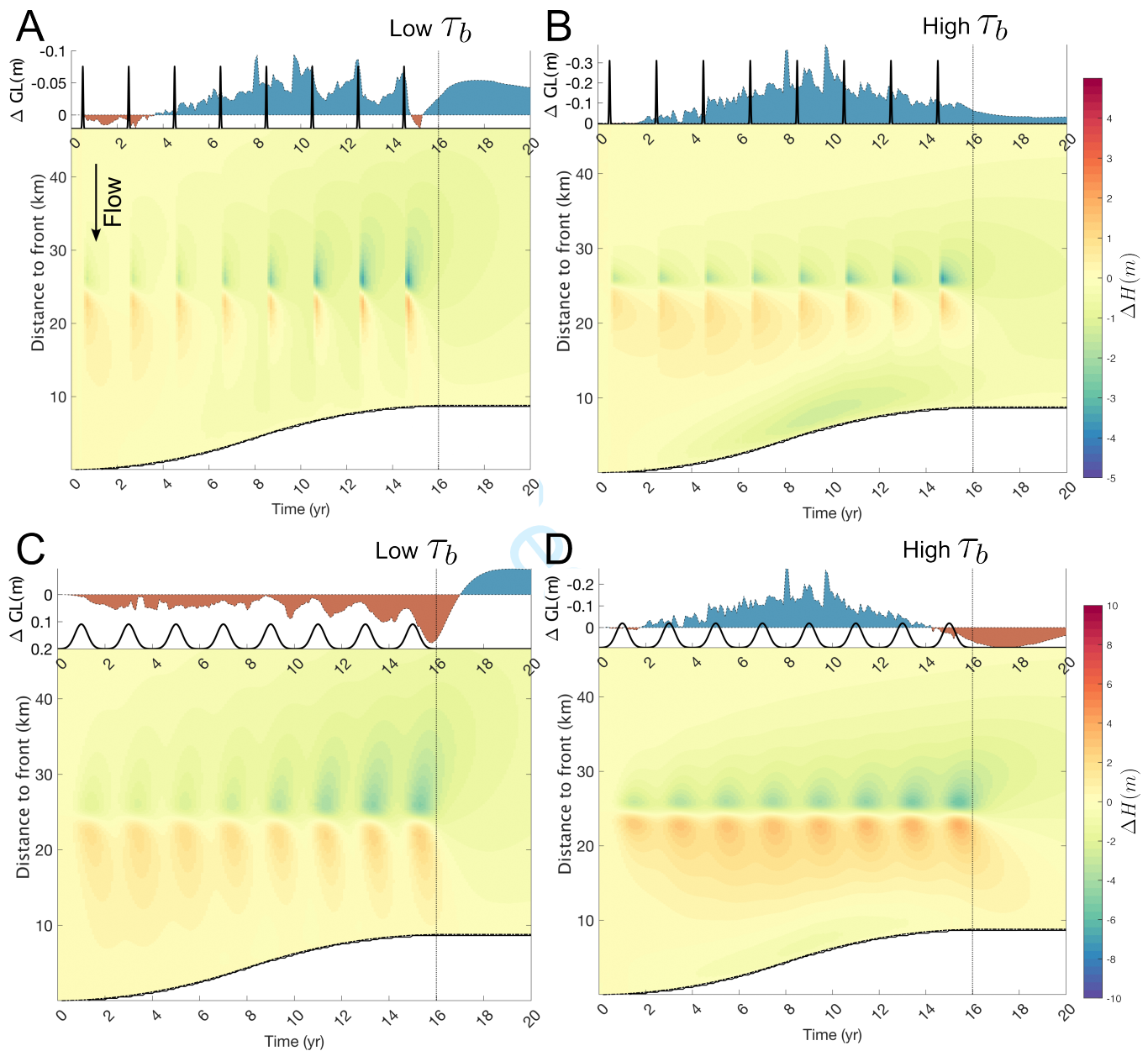


**Fig. 12.** Spatio-temporal pattern of dynamic thickness change along the center flow line at **narrow** and **shallow** testbed glaciers in response to the two types of localized basal perturbation pulses. All testbed glaciers remain almost fully grounded and hence the fronts and grounding lines overlap on the plots. Graphic features and subplot arrangements are the same as Fig. 4.



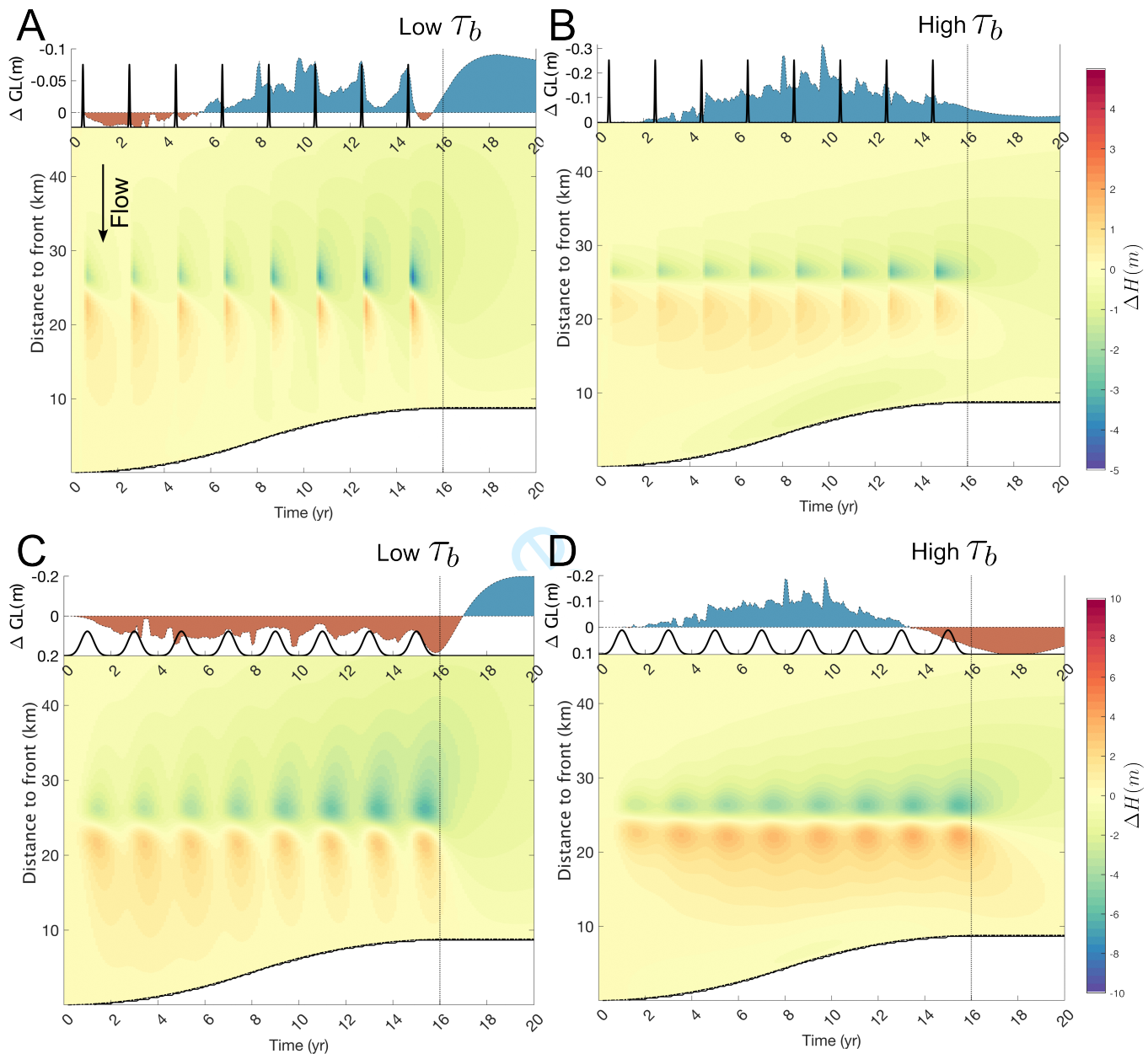


**Fig. 13.** Spatio-temporal pattern of dynamic thickness change along the center flow line at **wide** and **shallow** testbed glaciers in response to the two types of localized basal perturbation pulses. All testbed glaciers remain almost fully grounded and hence the fronts and grounding lines overlap on the plots. Graphic features and subplot arrangements are the same as Fig. 5.

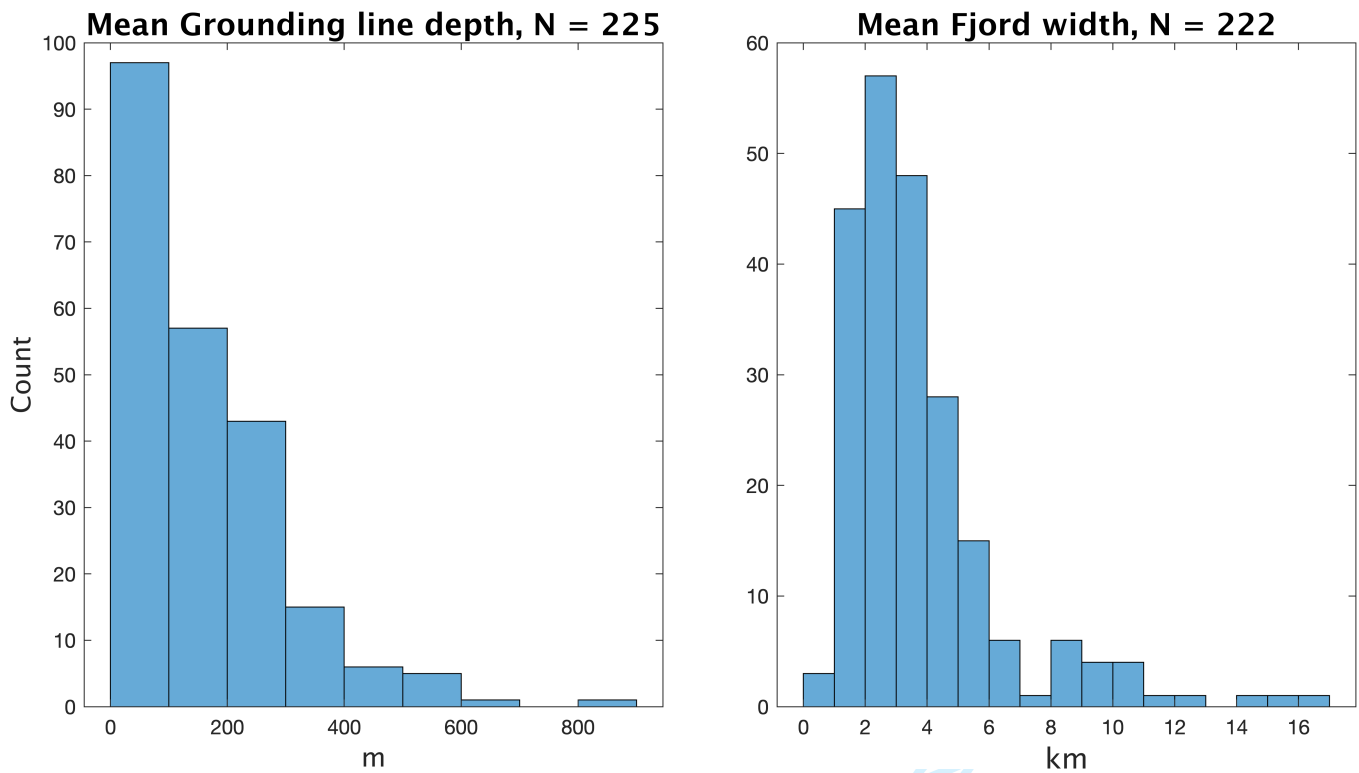


**Fig. 14.** Distributions of mean fjord width and grounding line depth in observational data around most of the Greenland outlet glaciers, plotted from Wood and others (2021).  $N$  is the total number of available glacier data in the original study.